Stony Brook University

Fluid Structure Interaction (FSI) for Evaluation of Biomedical Implant Devices for Novel Hypertension Treatment Therapy

A Thesis Presented

by

Dinesh Amirtharaj Peter

to

The Graduate School

in Partial Fulfillment of the

Requirements

for the Degree of

Master of Science

in

Biomedical Engineering

Stony Brook University

August 2011

Stony Brook University

The Graduate School

Dinesh Amirtharaj Peter

We, the thesis committee for the above candidate for the

Master of Science degree, hereby recommend

acceptance of this thesis.

Danny Bluestein, Ph.D. – Thesis Advisor
Professor of Biomedical Engineering

Yi-Xian Qin, Ph.D. – Chairperson of Defense Committee
Professor of Biomedical Engineering

Helmut H. Strey, Ph.D.
Associate Professor, Graduate Program Director of Biomedical Engineering

Nicos Labropoulos, Ph.D., RVT
Professor of Surgery

This thesis is accepted by the Graduate School

Lawrence Martin
Dean of the Graduate School

Abstract of the Thesis

Fluid Structure Interaction (FSI) for Evaluation of Biomedical Implant Devices for Novel Hypertension Treatment Therapy

by

Dinesh Amirtharaj Peter

Master of Science

in

Biomedical Engineering

Stony Brook University

2011

Drug-resistant hypertensive patients may be treated by mechanical stimulation of stretch-sensitive baroreceptors located in the sinus of carotid arteries. To evaluate the ability of custom devices to stretch the carotid sinus such that the induced stretch might trigger baroreceptors to increase action potential firing rate and thereby reduce hypertension, numerical simulations were conducted of several biomedical implant devices deployed in subject based carotid models. Two different carotid models were chosen to serve as virtual vascular environment for device deployment evaluation - a physiologic model and a diminutive non-physiologic model. Extravascular and endovascular device designs, custom built for the carotid models, were also chosen for evaluation. An augmented FSI with contact surface implemented methodology was used to conduct simulations. Results indicated that endovascular devices stretch carotid sinus more efficiently compared to extravascular devices. Effects of endovascular device deployment were evaluated on extreme carotid models and carotids under pathological conditions. These evaluations were conducted to test the limits of our numerical methodology and also to predict the response that such devices would elicit under various biological conditions. From the context of numerical simulations, endovascular devices consistently induced significant carotid sinus stretch, in all cases, thereby indicating that these devices might have a long lasting effect on reducing resistant hypertension.

Table of Contents

List of Tables

List of Charts

List of Figures

List of Abbreviations

CCA	Common Carotid Artery
ICA	Internal Carotid Artery
ECA	External Carotid Artery
MAP	Mean Arterial Pressure
DEG/ENaC	Degenerin/Epithelial Na^+ Channel
NTS	Nucleus of Solitary Tract
EAA	Excitatory Amino Acid
NMDA	N-methyl-D-aspartic acid
CVLM	Caudal Ventrolateral Medulla
GABA	Gamma-aminobutyric Acid
RVLM	Rostral Ventrolateral Medulla
IML	Intermediolateral Nucleus
FSI	Fluid Structure Interaction
ALE	Arbitrary Lagrangian Eulerian
WSS	Wall Shear Stress

Acknowledgments

I would like to thank my advisor, Dr. Danny Bluestein, for having given me the opportunity to work on this project. His continued guidance and support have helped me get through my graduate research successfully. I consider it an honor and privilege to have worked for such a big name in the field of numerical simulations. I am especially thankful to employees of Vascular Dynamics Inc., Israel – Ori Weisberg, Dr. Itzhak Avneri and Tal Oren, for their collaborative efforts.

I am indebted to Drs. Michalis Xenos and Yared Alemu, my simulation gurus, for their time, patience, moral and technical support. Without their guidance, this project would not have been possible.

Special thanks to Dr. Gaurav Girdhar, Dr. Jawaad Sheriff, Thomas Claiborne, Philip Chiu and Xuan Liang for making my stay in US a fun and memorable one. Prodigy affiliations of the lab – Suraj Rambhia and Sagar Rambhia – continue to amaze me with their talents. It was a pleasure knowing and working with all past and present members of Biofluids Lab.

Finally, what I am today and what I will be is because of my family – Peter, Nirmala Peter and Anila Shiny. Thank you for everything Dad, Mom and Shiny.

I. Introduction

Hypertension is the chronic condition of persistent elevated systemic blood pressure leading to grave cardiovascular pathologies and eventually death, if left untreated. Persons with blood pressure exceeding the standard threshold of 140/90 mm Hg are termed hypertensive and the condition has been found to be prevalent in 28% Americans [1]. It is responsible for approximately 7 million deaths annually world over [2] and treatment associated direct healthcare cost in the United States for the year 2001 has been estimated to be more than $54 billion [3]. First line of treatment in hypertension reduction is consumption of anti-hypertensive drugs combined with changes in lifestyle and diet regimen of patient. Despite following drug treatment for sufficient treatment periods, some patients do not respond to medication resulting in persistence of hypertensive conditions. Such a non-responsive hypertensive condition is deemed as resistant hypertension if the patient fails to respond to at least three drug therapies prescribed by the physician, one of which is a diuretic meant for high blood pressure [4]. Primary cause alluded to resistant hypertension is non-compliance of the patient's body to anti-hypertensive drugs, amongst other factors such as secondary hypertension and internal resistance to treatment [5]. Obesity, physical inactivity, excessive alcohol consumption and high sodium intake via salt consumption through various dietary means are factors that augment the body's drug therapy resistance capacity. As an alternative to drug therapy for treating resistant hypertension, activation of the patient's carotid baroreceptors by stretching carotid sinus, using implant devices, and thereby instigation of the carotid baroreflex began to be looked upon as an attractive therapeutic methodology.

This study pertains to evaluation of different biomedical implant devices and their efficiency in stretching carotid sinus, without adversely affecting other vascular biomechanics or hemodynamics, such that their deployment might induce a reduction in systemic blood pressure levels. The study is based on the central hypothesis:

Endovascular devices provide most improved arterial stretch response, compared to extravascular devices, without adversely affecting hemodynamics in both physiological and pathological cases.

This hypothesis is addressed by the following specific aims.

Specific Aims: Calculate wall biomechanics and vascular hemodynamics using fluid-structure interaction (FSI) methodology:

#1: To compare effects of extravascular and endovascular device deployment on physiologic carotid model

#2: To evaluate effect of endovascular device deployment on extreme carotid model

#3: To evaluate effect of endovascular device deployment on physiologic carotid model under pathological conditions

II. Background and Significance

Prior to delving into device based methodology to stimulate baroreceptors, the baroreflex mechanism for regulating blood pressure and anatomy of components involved in baroreflex are discussed below.

2.1 Anatomy of carotid artery

Carotid arteries, located on either side of the neck, are one amongst several arteries supplying oxygenated blood to the brain and face. Each carotid has a central common carotid artery (CCA) bifurcating into an internal carotid artery (ICA), supplying blood to the brain and a smaller external carotid artery (ECA), supplying blood to the face.

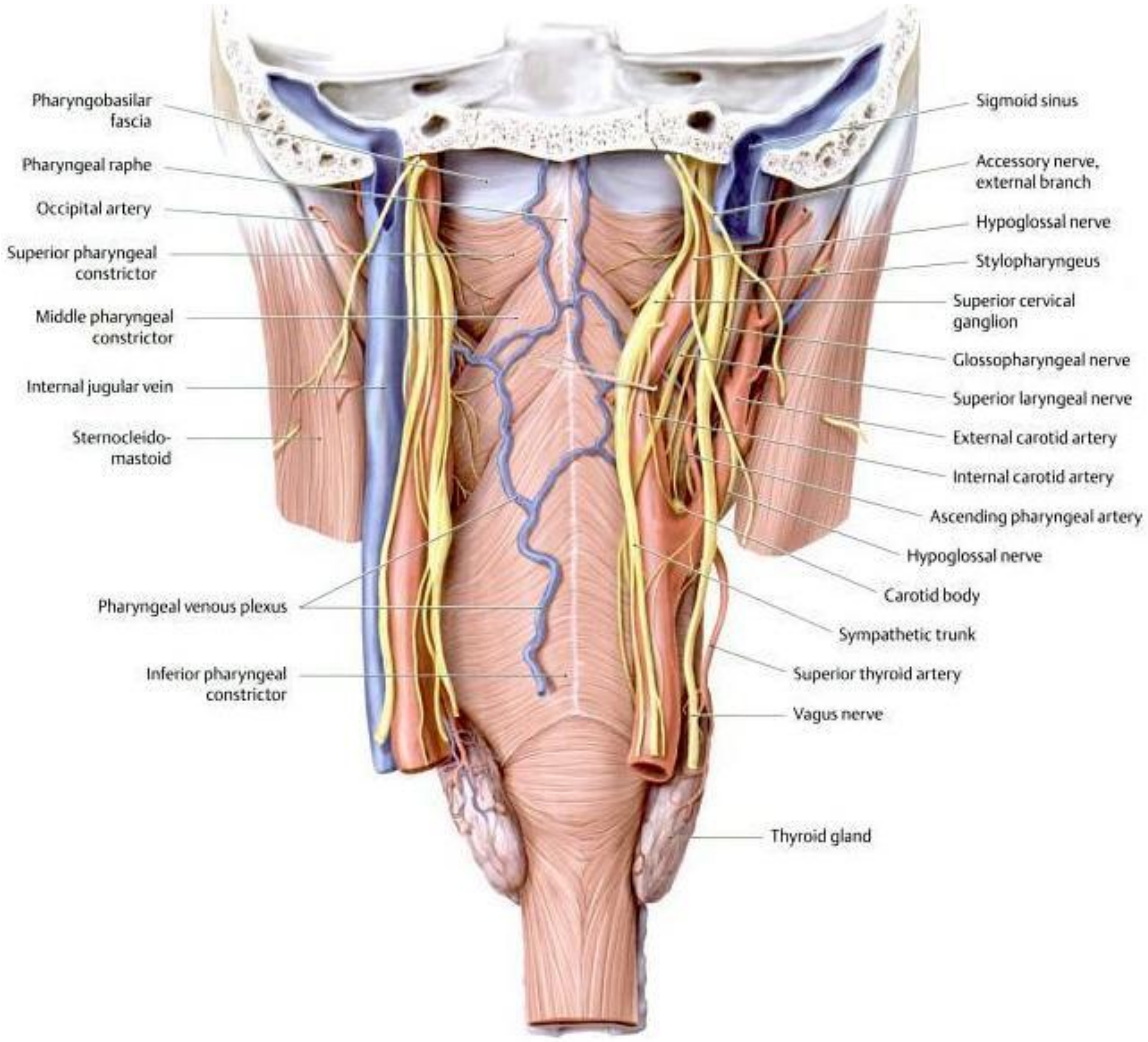

Figure 1. Anatomy of neurovascular structures located in neck [6]. Shown is the posterior view of parapharyngeal space with spinal column removed. Neurovascular structures on the left are

intact while those on the right side have been retracted for identification purposes. Carotid body has also been exposed, showing nerve innervations.

Anatomically, carotid sinus is the dilated region (distribution of which is shown in Fig 2) of internal carotid artery, at the bifurcation region, containing mechanosensitive baroreceptor nerve endings. The sinus is a specialized elastic region composed of a thinner tunica media and a thicker tunica adventitia (or externa) [7, 8]. This variable tissue composition enhances elasticity and area of sinus compared to segments of the artery adjacent to it.

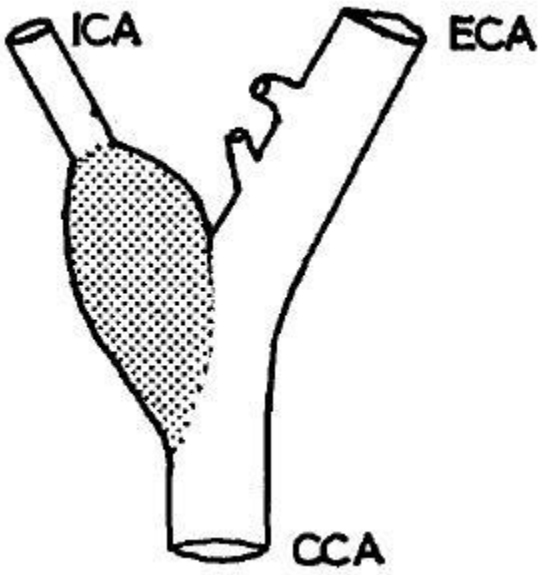

Figure 2. Artistic interpretation of the specialized elastic region distribution, representing the carotid sinus, in a human carotid bifurcation [9]. Legend: ICA – internal carotid artery, ECA – external carotid artery, CCA – common carotid artery.

Baroreceptor is an umbrella term, encompassing all stretch-sensitive receptors located in the carotid sinus and aortic arch. These receptors play a vital role in regulation of systemic blood pressure by responding to changes in arterial blood pressure. As the response of baroreceptors depend on the extent of vessel wall distension due to blood flow, any pressure change in the absence of wall deformation does not induce a suitable response [10]. Both static and pulsatile pressures elicit response from baroreceptors but the effect of stimulation is more in case of latter [11].

These baroreceptors receive blood pressure induced wall distension stimuli and pass on electrical impulses to the brain stem. At the sinus, not all baroreceptors get activated by stimuli at the same instant. They get recruited into responding to stimuli and passing on impulses as and when required.

Threshold for carotid baroreceptor activation is a mean arterial blood pressure (MAP) of 60 mm Hg. Aortic arch baroreceptors have a much greater threshold value (95 mm Hg) for activation [7] and function only as 'second-in-line' to carotid baroreceptors in systemic blood pressure regulation. Principal reason for the difference in threshold values for activation between carotid and aortic baroreceptors is attributed to the difference in arterial wall compositions at the locations of the two arterial baroreceptors. Carotid baroreceptors are found in the specialized region of carotid artery where the arterial wall is made up of less muscle tissue and more collagen compared to the adjacent common carotid artery [12, 13] while aortic baroreceptors are located in a region of aortic arch which is not significantly different in composition compared to its immediate surroundings. Smooth muscles cells have been found to be infrequent at the location of aortic baroreceptors and the specific type of smooth muscle cells occurring in those regions have been characterized to be of spannmuskeln type, which even upon stimulation, elicits inconsequential changes in arterial wall diameter, if any [14]. Above the mentioned threshold value of 60 mm Hg, carotid baroreceptors begin firing action potentials, the frequency of which increases with increase in blood pressure and reaches its peak at 180 mm Hg, beyond which the firing rate plateaus out. Sensitivity of baroreceptors, to respond to blood pressure changes, is at its maximal at MAP of approximately 95 mm Hg and any small deviations from this set value would result in significant variations in the frequency of action potential firing [15].

2.2 Nerves in baroreflex pathway and mechanism of baroreceptor activation

Baroreceptors are distributed along the tunica adventitia of carotid sinus and are innervated by nerve endings of a branch of the glossopharyngeal (cranial IX) nerve called Hering's nerve. Prior to innervating the carotid sinus, Hering's nerve bifurcates and supplies to the carotid body as well, which is an ovoid structure, present one on each side of the neck and tucked deep within the carotid bifurcation, functioning as chemoreceptors regulating respiration [16]. The aortic arch baroreceptors are innervated by aortic nerve, which ascends from the aortic

arch, combines with vagus nerve and finally terminates at the nucleus of solitary tract (NTS) of the brain stem where glossopharyngeal nerves from the carotid baroreceptors also terminate.

Several studies sought to understand the molecular structures responsible for converting mechanical stimuli to electrical signals at the adventitial section of the sinus. While some pursued the exploration of stretch-activated ion channels responsible for mechano-electrical transduction in baroreceptors [17-19], a particular study demonstrated that the non-voltage gated non-ligand gated amiloride sensitive depolarizing degenerin/epithelial Na^+ channel (DEG/ENaC) superfamily of ion channels play a significant role in the transduction of mechano-electrical impulses in arterial baroreceptors [20, 21]. Now, it has been demonstrated that the mechanotransduction process involves activation of two channels in tandem; mechanical stimulation causes depolarization through the non-voltage gated DEG/ENaC channels, resulting in generation of action potentials, followed by activation of voltage-gated ion channels at the spike initiating zones (shown in Fig 3) which results in firing of action potentials [22]. Action potential discharges triggered from the spike initiating zone on the terminal axons [23] propagate to the medulla oblongata of brain stem via glossopharyngeal and vagal nerves (which have their central processes terminating in the NTS) [24]. NTS recognizes variations in blood pressure depending on the frequency of incoming action potential signals. Effects of baroreceptor activation are reflected on the sympathetic and parasympathetic nervous systems. Components of these two nervous systems and mechanism in which they are instigated to respond to blood pressure changes are detailed below.

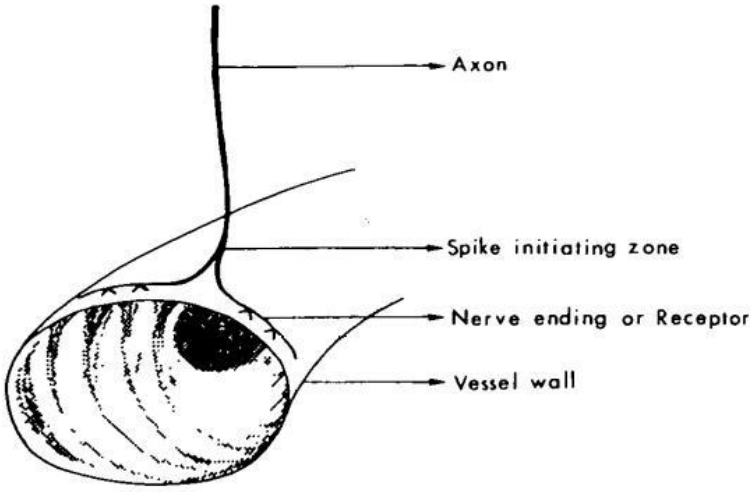

Figure 3. Artistic interpretation of the components of a baroreceptor showing nerve endings in the arterial wall as well as spike initiating zones where action potentials are fired from [25].

2.3 Components of the sympathetic branch of baroreflex

Baroreceptor afferent branches arriving at the NTS have an excitatory effect and release glutamate, an excitatory amino acid (EAA), which then binds monosynaptically on non-NMDA [N-methyl-D-aspartic acid] glutamate receptors and polysynaptically on NMDA and non-NMDA receptors, opening up ion channels and enhancing neuronal activity [26, 27]. Thus, the synapse between afferent branches and the cell bodies of NTS is an excitatory synapse which employs glutamate as its neurotransmitter [28-30]. Processing of baroreceptor information at NTS takes place with a variety of input, from other afferent branches especially the hypothalamus and cortex of brain, evoking a modulatory response rather than a completely inhibitory or excitatory effect [31].

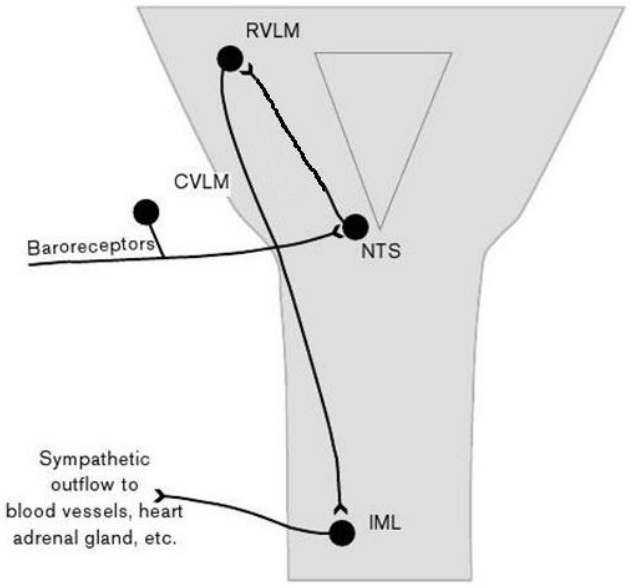

Figure 4. Schematic of the major pathways involved in sympathetic baroreceptor reflex [31]. Legend: RVLM – rostral ventrolateral medulla, CVLM – caudal ventrolateral medulla, NTS – nucleus tractus solitarius, IML – intermediolateral nucleus.

Caudal ventrolateral medulla (CVLM) is the site at which excitatory baroreceptor inputs from NTS are converted to an inhibitory effect on sympathetic activity [32, 33]. CVLM, made up of a rostral group of neurons that release GABA as neurotransmitters [34], is “tonically active” even in the absence of baroreceptor input [35, 36]. CVLM is connected to the rostral ventrolateral medulla (RVLM) via sympathoinihibitory interneurons (SIN) whose axons project

rostrally and bilaterally from CVLM to RVLM, and they synapse onto several different types of bulbospinal neurons in the RVLM [37, 38]. RVLM is subject to input from both inhibitory and excitatory inputs. Thus, the net sympathetic effect from RVLM is a balance of both inputs. Both CVLM and RVLM are located in the medulla while the subsequent site of interest in the baroreflex pathway, the intermediolateral nucleus (IML) is located in the spinal cord. The IML receives dense innervation from the C1 catecholamine group of neurons in the RVLM [39]**.** Fibers of the sympathetic preganglionic nerves of the efferent pathway, innervating both heart and smooth muscle cells, originate from IML [40].

2.4 Components of the parasympathetic branch of baroreflex

As part of the parasympathetic branch, NTS supplies axons to the bilateral vagal nuclei. Vagal preganglionic fibers, responsible for heart rate manipulation, originate from the two vagal nuclei, dorsal motor nucleus of vagus and nucleus ambiguus, both of which are located in medulla oblongata [41] and innervate the heart separately from sympathetic preganglionic nerves. These preganglionic nerves terminating at the heart complete the parasympathetic efferent branch of arterial baroreflex.

Thus, the overall components making up carotid baroreflex are the sensory receptors, afferent nerves, integration centers in the central nervous system, efferent nerves (both sympathetic and parasympathetic) and effector organs which includes heart and peripheral vessels.

2.5 Mechanism of arterial baroreceptor reflex

An increase in blood pressure stretches the carotid sinus, which stimulates stretch-sensitive baroreceptors to fire action potentials in quick succession. Depending on the extent of arterial wall stretch, frequency of action potential fired from baroreceptors is increased, resulting in a proportional inhibition of sympathetic output and elevation of parasympathetic activity. Decreased sympathetic output slows down heart rate, decreases cardiac contractility and also suppresses blood flow to capillaries (arteriolar tone) thereby affecting blood volume in small veins and venules (venous tone). Reduced arteriolar tone causes vasodilation resulting in a drop in the total peripheral resistance while reduced venous tone causes a drop in peripheral venous pressure. A decrease in venous pressure and cardiac contractility together influence the cardiac

stroke volume to drop, which when combined with a slow heart rate reduces mean arterial pressure (MAP). Meanwhile, parasympathetic activity has an inverse effect on heart rate. An elevation of parasympathetic activity reduces heart rate thereby lowering cardiac output and eventually arterial pressure. Thus, arterial blood pressure reduction is the net effect of all effector organs involved in the baroreflex pathway.

Activities of all nerves and output of the effector organs are completely reversed in case of arterial pressure drop. Systemic response to effects of such a negative feedback mechanism occurs within a few seconds from the reception of stimuli at the baroreceptor nerve endings. Cardiac response for stimuli is reported to be maximal in one or two heart beats after stimuli while response from peripheral vascular vessels in the form of vasodilation or vasoconstriction is maximal at 10-15 seconds [42]. Thus, baroreflex manipulates heart rate on a beat-to-beat basis more via parasympathetic activity than sympathetic activity [43].

2.6 Orthostatic hypotension

Under homeostatic conditions, baroreflex pathway works to restrict systemic blood pressure from dropping to hypotensive levels, than preventing a rise in pressure. However, sudden postural changes such as a quick rise from lying down position might result in immediate drop in blood pressure and could cause momentary dizziness, blurriness of vision etc. Such a condition, termed orthostatic hypotension, occurs due to blood accumulation in the veins of ankles and legs as a result of gravitational forces. This gravity-effected blood pooling lowers venous return to heart, thereby lowering cardiac output and subsequently blood pressure. This fall in blood pressure is immediately regulated by baroreceptors which trigger enhanced vasoconstriction as part of baroreflex feedback mechanism, thereby increasing the total peripheral resistance and subsequently systemic blood pressure.

2.7 Baroreceptor activity during exercise

During exercise sessions, though heart rate and blood pressure levels are elevated, baroreceptors have been found to be effective and have been proven to regulate arterial blood pressure [44, 45] by resetting to an elevated ‘operating point’ pertinent to blood pressure levels prevailing then [46, 47]. At rest, heart rate is controlled predominantly by parasympathetic activity, as mentioned earlier. However, as heart rate increases and crosses 100 beats per minute

during exercise, activity of the sympathetic branch nerves is enhanced while vagal tone is decreased. During very high heart rates, there is total suppression of vagal outflow (parasympathetic activity) [46]. Ogoh *et al.* have demonstrated that, at rest, one third of arterial blood pressure changes as part of the baroreflex are due to heart rate and cardiac output changes while the remaining two-thirds are due to changes in vascular resistance. As intensity of exercise increases, contribution of vascular resistance to maintenance of blood pressure increases while those of cardiac output decreases [46].

2.8 Baroreceptor resetting – adaptation to altered blood pressure levels

An increase or decrease in arterial blood pressure is immediately reflected by a corresponding change in the frequency with which action potentials are fired from baroreceptors. However, studies have observed that in chronic hypertensive cases the firing rate of action potentials at elevated blood pressure levels is the same as the rate at which they are fired in normotensive state [48], thereby indicating baroreceptors might adapt to altered blood pressure levels as baseline for activation. Such resetting could either be due to adaptation at the baroreceptor level, at the central nervous system resulting in altered coupling between afferent input signals and efferent output responses, or adaptation at the effector organ level [49]. Thus, the change in relation between arterial blood pressure and sympathetic or parasympathetic activity affecting heart rate and peripheral vascular resistance could be due to resetting of baroreceptors or any other component of arterial baroreflex. Decreased compliance of vessel wall with progression of age, wall structural changes due to pathologies such as increased collagen content during chronic hypertension, inadvertent activation of endothelium to release substances during wall stretch and viscoelastic property of arterial wall that non-uniformly distributes the tension due to stretching, are some of the factors attributed for baroreceptor adaption to altered stress levels [49] and such adaptive responses occur over a span of minutes to days from the onset of stimuli [50]. It is also observed that baroreceptors adapt readily to static pressures while resetting is subdued or completely absent when the elevated pressure is pulsatile [49, 51].

Though baroreceptors respond immediately to irregularities in arterial blood pressures with the objective of restoring blood pressure to baseline value, their adaptation, over a period of time to such altered pressure values led to belief in the notion that baroreceptors are fit only for

short-term regulation of blood pressure and not long-term regulations. However, recent studies of manual baroreceptor activation, detailed below, present evidence that baroreceptors and baroreflex do in fact have a long lasting effect on suppressing hypertension even in cases of chronic hypertension.

2.9 Device based therapeutic approaches for resistant hypertension

A few decades back, independent studies focused on stimulating carotid sinus as an alternative therapy for drug-resistant hypertension treatment [52-54]. Very recently, baroreflex was activated by electrical stimulation of carotid baroreceptors, the effect of which translated into an immediate fall of approximately 25 mm Hg MAP, associated reduction in heart rate and more importantly, sustenance of such effects over the entire period for which sinus was electrically activated [55, 56]. At the same time, a miniaturized implantable electronic device, Rheos (CVRx, Minneapolis, MN), designed for electrical stimulation has drawn attention for acceptable safety levels of implant procedure with low rate of adverse events and for generation of significant reduction in resistant hypertension [57, 58]. Alternately, a catheter-based approach for ablation of renal sympathetic nerves, which directly influence systemic blood pressure, is being looked upon as an attractive alternative to implant devices for hypertension treatment [59, 60].

Despite such progress in treating hypertension using novel device based therapeutic approaches, there is still plenty of scope for development of alternate treatment methodologies, primarily because the devices outlined above involve invasive procedures and substantiation of their effectiveness on large-scale clinical trials is still under progress. Thus, presented here are prototypes of mechanical implant devices, deployed in the sinus region of carotid artery, and numerical methodologies that evaluate effects of mechanically stimulating baroreceptors using such implants. Fluid structure interaction (FSI) simulations of custom implant devices deployed in patient based carotid bifurcation model are conducted to assess the ability of implants to stimulate baroreceptors and thereby reduce hypertension. In FSI, fluid and solid domains interact with each other at the interface of the two domains resulting in forces being applied onto the solid due to flowing fluid and the corresponding solid domain deformations affecting the hemodynamic conditions of fluid domain. Such domain coupled simulations facilitate non-invasive prediction of physiologic parametric values generated in the carotid artery due to

implant deployment. To the best of my knowledge, this is the first time that FSI methodology has been implemented for analyzing a fully coupled dynamic interaction between three domains - arterial wall, fluid domain and deployed stent - to quantify the effects of device deployment. Apart from evaluating the ability of implants to stretch carotid sinus, the FSI methodology will ultimately aid in optimizing designs of mechanical devices such that the most efficacious designs could be manufactured and subject to animal trials.

III. Research Design

Quantifying the effects of device deployment involves three dimensional stress-strain analysis of carotid arterial wall and hemodynamic analysis of the volume of blood flowing through the artery. Geometric variations in the physiology of artery, non-uniform expansion of arterial wall due to blood flow, design of implant device, orientation of device deployment and extent of wall distension due to deployment result in spatial variation of stress and strain distribution on the arterial wall. Thus, for a comprehensive analysis of hypertension therapy using mechanical implants, FSI analysis of a subject based three dimensional model of carotid artery subject to stimulation by an implant device, custom made for the artery, is required.

Several simulations were conducted as preliminary studies to evaluate mechanical stimulation of baroreceptors on simplified carotid geometry. These were subsequently followed up by studies on subject based carotid models. As part of preliminary studies, a straight tube model (termed CA1, as in Carotid Artery 1) of carotid artery was subjected to arterial distension by an external device.

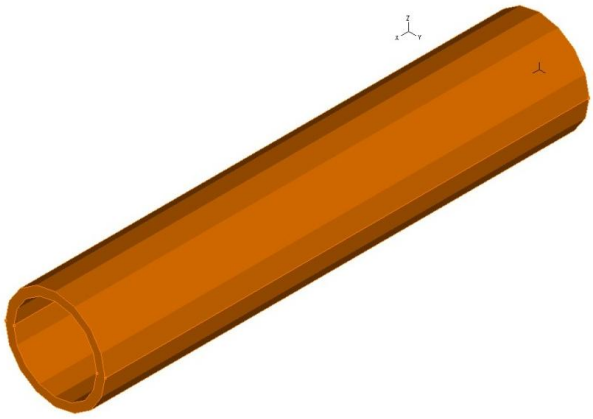

Figure 5. Simplified version of carotid artery. Nomenclature to be used henceforth for this geometry would be CA1. Dimensions of CA1: internal diameter - 6mm, outer diameter - 7.2mm, length - 35mm.

Two square blocks (termed D1, as in Device 1) were placed diametrically outside the artery and made to compress it.

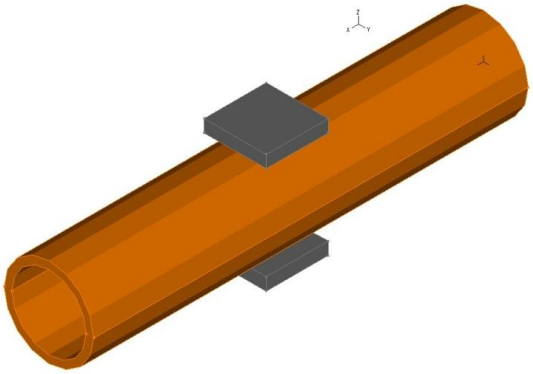

Figure 6. Prototype stenotic devices, in the form of square blocks (D1). Dimensions of one square block: length - 5mm, breadth - 5mm, height - 1mm.

Custom made extravascular stenotic devices of slight variations in design (D2 and D3) replaced the two square blocks (D1) in subsequent studies.

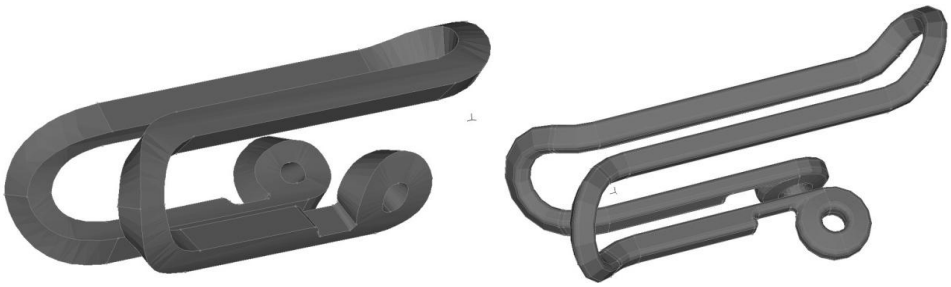

Figure 7. Custom stenotic devices - design D2 is shown on the left while modified version of D2 is shown on the right (D3). Dimensions for both designs: internal diameter - 4mm, thickness - 1mm, length - 17mm.

Straight tube model of carotid artery was replaced by a patient specific geometry (CA2) which was stimulated by a completely different extravascular device design (D4).

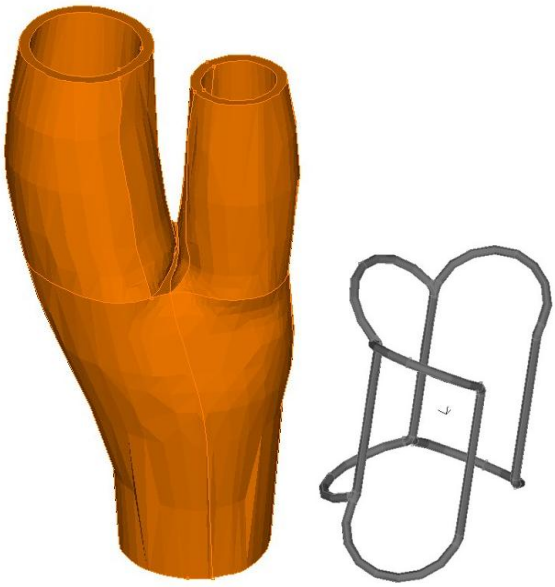

Figure 8. Subject based carotid model shown on the left with extravascular stenotic device on the right. Dimensions of CA2: Height - 44mm, internal diameter at CCA - 9.5mm, at ICA - 8.3mm, at ECA - 5.3mm, wall thickness - 1mm. Dimensions of D4: Height - 11.7mm, internal diameter - 7.3mm, thickness - 0.4mm.

Extravascular stenotic devices were replaced, in subsequent studies, by intra-luminal stents which were deployed in the sinus region of ICA. Shown below is the first stent design (D5).

Figure 9. Intra-luminal stent design, in crimped state, employed to distend vascular wall from within the sinus. Dimensions of D5: Height - 17mm, internal diameter - 6.6mm, thickness - 0.2mm.

Stent design D5 was modified to be more compact and to fit in patients with narrow sinus regions. Modified stent (D6) is shown below.

Figure 10. Modified version of stent (D6) in crimped state. Dimensions of D6: Height - 13mm, internal diameter - 2.8mm, thickness - 0.2mm.

A case study was conducted with stent design D6 deployed in another carotid geometry (CA3), which was smaller in dimensions and more streamlined, compared to CA2, with branches of the bifurcation aligned almost parallel to each other as shown in Fig 11. While the first subject based carotid CA2 was representative of the gamut of physiologic carotid models in terms of geometry and dimensions, this smaller carotid was chosen for evaluation of effects of stent deployment on an extreme case of carotid bifurcation geometry and its possible effects on flow in a bifurcation which widely departs from the normal physiologic geometry.

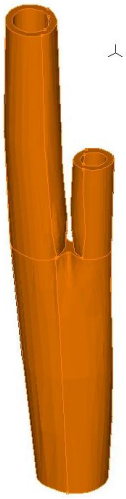

Figure 11. Second subject based carotid model (CA3). Dimensions of CA3: Height from CCA to ICA exit - 53mm, from CCA to ECA exit - 38mm, internal diameter at CCA - 5.5mm, at ICA - 3.8, at ECA - 2.4mm, wall thickness - 0.6mm.

IV. Methods

Subject based carotid artery model CA2 (courtesy of Dr. Steinman, University of Toronto [61]), procured in surface meshed format, was converted to volumetric geometry using CFD pre-processing package Gambit (ANSYS Inc, Canonsburg, PA). Lumen volume was also created using Gambit, with arterial wall as volumetric reference. The geometries created consisted of lumen and artery wall as separate bodies. Care was taken to ensure that the created volumes had sufficient entry length for blood flow. The second carotid model CA3 and all device geometries were procured in parasolid volumetric format from Vascular Dynamics Inc, Herzelia, Israel. The procured second carotid CA3 was smaller in dimensions and more streamlined compared to the physiologic model CA2. Straight tube model of carotid and the stenotic square block devices, used in preliminary studies, were created in Gambit. Discretization of all created carotid volumetric geometries and procured device geometries was carried out using finite element analysis software package ADINA (ADINA R&D Inc, Watertown, MA) implementing first order four node tetrahedral meshing scheme.

4.1 Material Models

Arterial wall was modeled as a homogeneous, incompressible, non-linear, hyperelastic material defined by isotropic Mooney-Rivlin strain energy formulation [62]:

$$W = c_1(I_1 - 3) + c_2(I_2 - 3) + D_1[\exp(D_2(I_1 - 3)) - 1] \quad (1)$$

$$I_1 = \sum C_{ii}, \; I_2 = \frac{1}{2}[I_1^2 - C_{ij}C_{ij}] \quad (2)$$

where I_1 and I_2 are the first and second strain invariants, $C = [C_{ij}] = X^T X$ is the Cauchy-Green deformation tensor, $X = [X_{ij}] = [\partial x_i / \partial a_j]$, (x_i) is current position and (a_j) is original position of the deformation tensor. Material constants in Eqn. (1) were fitted with the following numerical values: C_1 = 36800Pa, C_2 = 0, D_1 = 14400Pa, D_2 = 2 [62]. Eqn. (1) and the numerical constants were used to generate the Mooney-Rivlin material behavior curve shown in Chart 1.

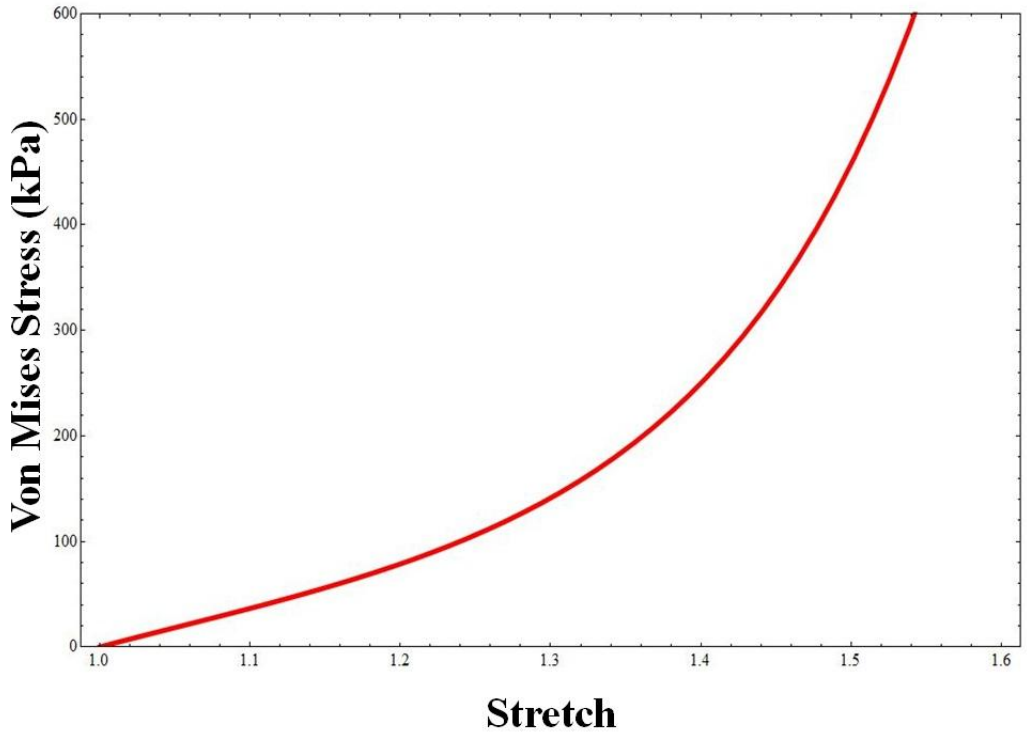

Chart 1. Von Mises stress-stretch behavior of the defined Mooney-Rivlin material model

Fluid domain was modeled as Newtonian fluid with laminar flow profile and ρ=1.056 g/cc, μ=3.5cP [63]. Flow was governed by both continuity and Navier-Stokes equations, which are presented below.

Continuity (conservation of mass):

$$\frac{\partial \rho}{\partial t} + \nabla \bullet (\rho v) = 0 \qquad (3)$$

where, ρ is density of fluid, v is velocity vector and t is time.

Blood was modeled as incompressible fluid. Accordingly, eqn. (3) is re-written as:

$$\rho \nabla \bullet v = 0 \qquad (4)$$

Simplified version of Navier-Stokes with gravitational and centrifugal forces neglected:

$$\rho(\frac{\partial v}{\partial t} + v \bullet \nabla v) = -\nabla p + \mu \nabla^2 v \qquad (5)$$

where, μ is viscosity of fluid.

Implant devices were modeled as stainless steel (E=193GPa, ν=0.45 and ρ= 8 g/cc) [64]. Contact surface feature was activated to model the interaction between implant and arterial wall.

Constraint-function algorithm [65], which was implemented, enforced frictional contact and prevented inter-penetration between contacting surfaces.

Equation dictating contact between two bodies was the principle of virtual work [66]:

$$\sum_{L=1}^{2}\int_{{}^{t}V} {}^{t}\tau_{ij}\delta_{t}e_{ij}\,d\,{}^{t}V = \sum_{L=1}^{2}\{\int_{{}^{t}V}\delta u_i\,{}^{t}f_i^{B}\,d\,{}^{t}V + \int_{{}^{t}S_f}\delta u_i^{S\,t}f_i^{S}\,d\,{}^{t}S\} + \sum_{L=1}^{2}\int_{{}^{t}S_c}\delta u_i^{c\,t}f_i^{c}\,d\,{}^{t}S \qquad (6)$$

In eqn. (6), for each contacting body i and j, ${}^{t}V$ is volume of body, ${}^{t}\tau_{ij}$ are Cauchy stress tensor components, $\delta_t e_{ij}$ are virtual strain components corresponding to δu_i imposed virtual displacements, ${}^{t}f_i^{B}$ are components of externally applied force per unit volume of body, ${}^{t}f_i^{S}$ are known externally applied surface traction components which act on surface area ${}^{t}s_f$ and ${}^{t}f_i^{c}$ are components of unknown contact tractions acting on the unknown and to be calculated area of ${}^{t}s_c$. Conditions for normal contact were dictated by

$$g \geq 0;\ \ \lambda \geq 0;\ \ g\lambda = 0 \qquad (7)$$

where g is gap function for the contact surface pair and λ is normal traction component of the contact tractions existing between two contacting bodies. Mathematical representation of Coulomb's law of friction was incorporated as follows, separately into the conditions to account for frictional conditions.

$$|\tau| \leq 1 \text{ and } |\tau| < 1 \text{ implies } \dot{u} = 0 \qquad (8)$$

In eqn. (8), $\dot{u}$ is tangential velocity relative to unit tangential vector at a point on one body which is in contact with another body, τ is a non-dimensional variable, defined by $\tau = \frac{t}{\mu\lambda}$ where t is time and $\mu\lambda$ is frictional resistance.

Numerical solution for the contact between two bodies was the solution of virtual work equation (6), subject to conditions of eqns. (7) and (8).

4.2 Boundary Conditions

Solid domain boundary conditions were complete displacement fixity for inlet face of ICA and axial translation for exit faces of ICA and ECA, which were applied to stretch the entire arterial wall and thereby emulate the tension and pre-stress conditions inherent in physiologic

arteries. Inner walls of the artery, that would contact the fluid domain, were marked as FSI interfaces. Boundary conditions for devices were specific to the type of device. For the extravascular device deployed on subject based carotid model, the two vertical central struts that hold together the remaining two struts by means of curvilinear frames were completely fixed while the other struts were permitted partial radial displacement. For stent type devices, expansion of the crimped stent was simulated by applying radial displacement on all four vertical struts.

Fluid domain boundary conditions were pressure at CCA inlet and velocity waveforms at ICA and ECA outlets. Time dependent pulsatile pressure waveform, representing systemic blood pressure of a normotensive person and in the range of 108/77 mm Hg [67], was applied as inlet boundary condition. Patient specific mass flow rates of fluid exiting from ICA and ECA, referenced from [67] were converted to corresponding velocity waveforms and applied as outlet boundary conditions. Null slip and FSI interface boundary conditions were defined for the faces of fluid domain that interacted with arterial wall. As the entire system was at zero stress initially, pressure and velocity waveforms were ramped up to their corresponding initial states of the cardiac cycle in a timeframe of 1 second. Following ramping up, simulations were carried out for two cardiac cycles.

4.3 Fluid Structure Interaction

Interactions between fluid domain and the encapsulating solid domain were analyzed using FSI methodology. A general Lagrangian formulation was employed for solid domain response while an arbitrary-Lagrangian-Eulerian (ALE) formulation was used for fluid domain [68]. At the FSI interfaces, displacement compatibility and traction equilibrium conditions, pertaining to the two domains were imposed, from which velocity at the fluid nodes and corresponding fluid traction, exerted on the solid domain, were calculated [69]. All FSI simulations were performed on high performance computing cluster composed of four quad core Xeon CPUs with a shared memory of 64 GB RAM. Grid independency of results was ensured for the simulations conducted. Simulations that produced less than 5% difference in stress and hemodynamic values for varying mesh densities were chosen. Results presented in this article pertain to mesh densities in Table 1.

Design Name	Design Description	Mesh Density		Total Number of Mesh Elements	
		Wall	Lumen	Wall	Lumen
CA1	Straight tube model of carotid	0.3mm	0.35mm	136,000	44,000
CA2	First patient specific carotid artery	0.7mm (2 layers)	0.75mm	153,000	74,000
CA3	Second patient specific carotid artery	0.3mm	0.3mm	133,000	103,000
		Device Mesh Density		Total Mesh Elements in Device	
D1	Square blocks stenotic device	0.9mm		2,700	
D2	Clip-shaped stenotic device for straight tube carotid	0.3mm		11,600	
D3	Modified version of stenotic device D2	0.3mm		13,200	
D4	Stenotic device for patient specific carotid	0.8mm		4,300	
D5	Intraluminal stent	0.15mm		7,100	
D6	Modified intraluminal stent	0.15mm		4,300	

Table 1. Mesh density and total number of tetrahedral mesh elements employed in simulations

Post-simulation, compliance of arterial wall [70] was calculated based on:

$$Stiffness(\beta) = \frac{\ln(Ps / Pd)}{(Ds - Dd) / Dd} \quad (9)$$

$$Compliance = \frac{1}{\beta} \quad (10)$$

where, *Ps* and *Pd* are systolic and diastolic blood pressure levels, *Ds* is maximum systolic diameter and *Dd* is minimum diastolic diameter. Several diameter measurements were taken at the sinus, and an average diameter was used in compliance calculation.

V. Numerical Evaluation of Carotid Implants for Hypertension Treatment

5.1 Preliminary Data: Evaluation of Effects of Stenotic Devices on Simplified Model of Carotid Artery

5.1.1 Case Study 1

Objective of this preliminary study was to use FSI coupled with contact surface methodology on simplified models of carotid artery subject to compression by extravascular stenotic devices, such that the results of simulation may help anticipate the effects that an actual implant would have on a physiologic carotid. Specifically, the study was conducted to anticipate effects of device deployment on the artery such as location of peak stress, behavior of Mooney-Rivlin material fitted carotid geometry model and response of flow domain to constriction.

5.1.1.1 Device Configuration

Carotid model CA1 was subject to stenotic compression by device D1, wherein the two square blocks were placed diametrically opposite to each other as shown in Fig 6. Compressive load was applied on the two blocks to induce constriction on the artery.

5.1.1.2 Results

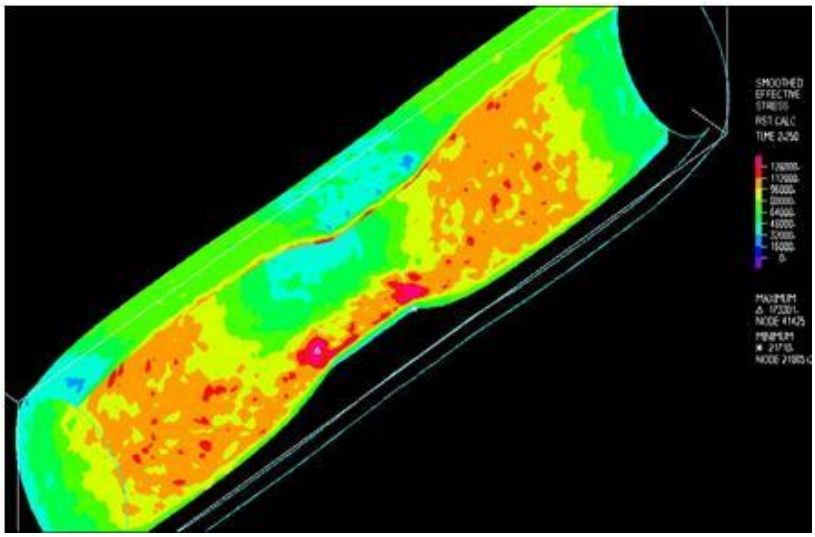

Figure 12. Stress distribution on a cross-section of artery constricted by device D1 is shown.

A cross sectional analysis of the stress distribution that developed due to constriction is presented in Fig 12. Stress was more uniformly distributed on either sides of the constriction, while at the constriction site itself, the effect of device was elicited by two distinct patches of high stress on the regions of arterial wall directly beneath the edge of device where arterial wall underwent maximum stretching. A peak stress of approximately 170 kPa was induced by the device on the wall.

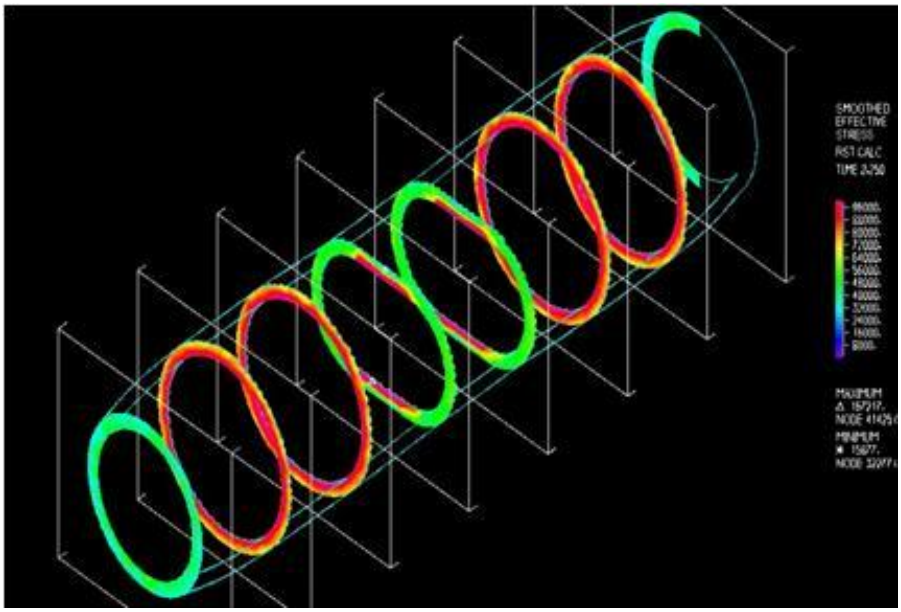

Figure 13. Planar view of stress distribution along axial direction of the constricted carotid

Biomechanical response of arterial wall to constriction is better illustrated by a planar view analysis of the shape that the artery assumed under constriction and the associated stresses that developed, as shown in Fig 13. The two central planes of the artery (shown in green in Fig 13) assumed a stadium shape [71] due to constriction while planes close to the proximal and distal ends assumed a more rotund shape with stresses uniformly distributed. At the planes chosen for pictorial representation (Fig 13), maximum stress was observed to be approximately 157 kPa. However, peak stress at the central planes remained at 170 kPa.

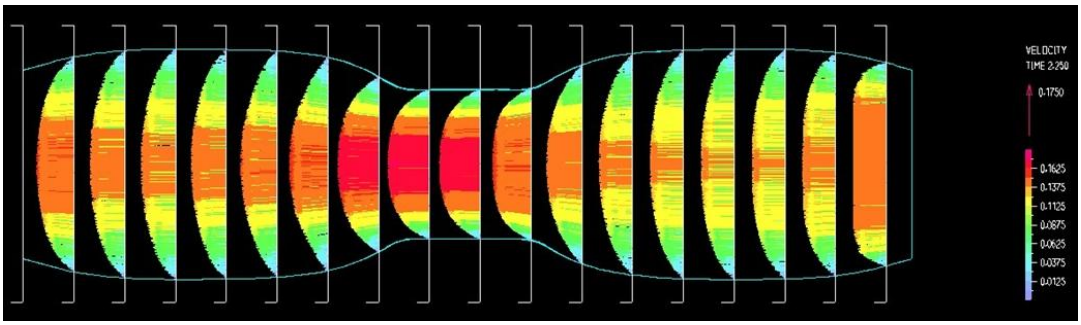

Figure 14. Velocity vector analysis at several cross-sections along axis of flow field. Flow direction is from right to left. Peak velocity occurs at the stenotic region, as indicated in red.

Associated hemodynamic response to constriction by an external device was an increase in velocity at the stenotic region, as shown in Fig 14. Cross sectional analysis of the velocity vector indicated that flow at the entry was not fully developed as depicted by plug flow profile. However, flow developed into parabolic profile as it passed through the vessel wall. The fully developed center-line velocity increased to 17.5 cm/s as flow area decreased.

5.1.1.3 Discussion

This study presented numerical evaluation of the effects of a constricting device on Mooney-Rivlin material fitted simplified carotid geometry. The study demonstrated the viability of FSI coupled with contact surface methodology in predicting locations of device induced peak stress as well as quantifying associated hemodynamics. Significant observation from the study was that high stresses developed in regions of arterial wall subject to enhanced distension such as the central planes shown in Fig 13. Solid lines of stress development observed in the two central planes were reflective of regions of arterial wall that underwent maximum stretch. Thus, the single most consequential deduction from simulation of a simplified model of carotid artery was that the device implant induced localized stretch at regions of contact with arterial wall, which translated into regions of elevated wall stress.

5.1.2 Case Study 2

Having gauged the constricting effects of a simple mechanical device on the arterial wall, the next objective was to compare the biomechanical response induced by prototypes of two stenotic devices of same dimensions but with slight design variations, on a simplified carotid

model. The goal was to evaluate the impact of design changes on the device's efficiency in mechanically stimulating baroreceptors.

5.1.2.1 Device Configuration

Straight tube model of carotid artery was fitted with stenotic devices D2 and D3, as shown in Fig 15, and evaluated as separate case studies. In order to emulate pre-stress conditions inherent in physiologic arteries, the carotid model was stretched to 10% its initial diameter. The stenotic devices, clamped to the artery, were designed to induce 30% radial compression at peak systole.

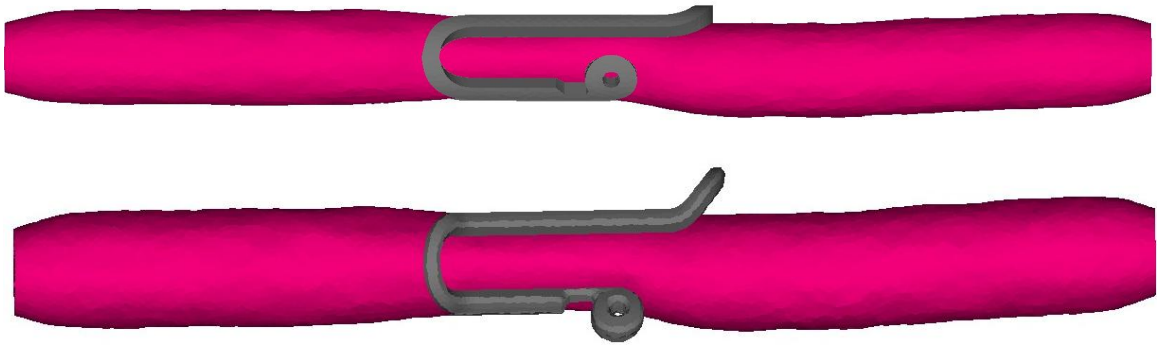

Figure 15. Carotid artery subject to 10% axial pre-stretch and 30% radial compression by stenotic devices D2 (top) and D3 (bottom).

5.1.2.2 Results

A comparative analysis of wall stress at the stenotic region showed that device D3 was more effective in inducing localized wall stress on the artery compared to D2. Evaluation of wall stress at several planes along the stenotic region revealed that D3 induced 4-16% more stress than D2. To compensate for the constricting effects of device, artery wall up and downstream of the stenosis underwent radial expansion augmented by fluid flow. As radial wall stretching was more up and downstream compared to stenotic region, elevated wall stresses were observed in those regions of the arterial wall. However, as stresses at regions other than the stenosis have no clinical significance pertaining to baroreceptor activation, they were not considered for analysis.

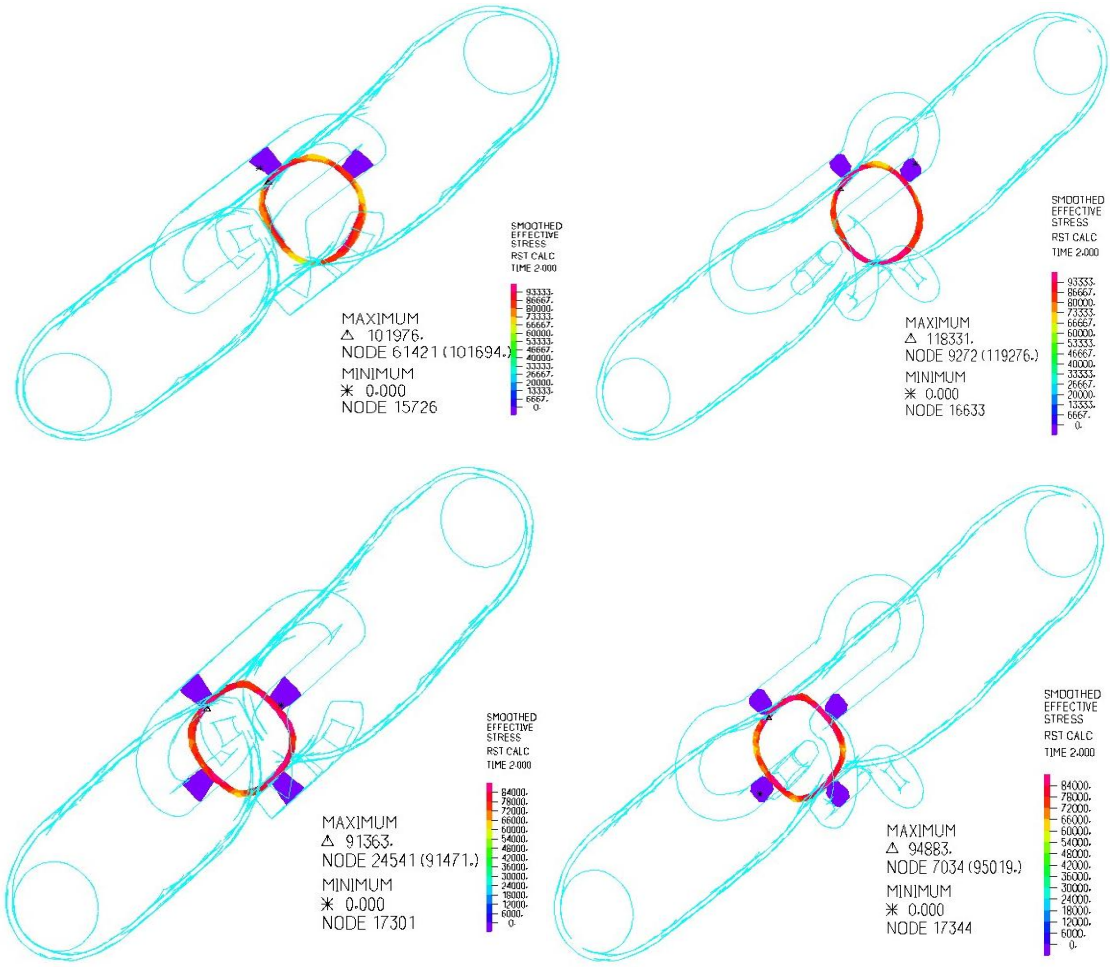

Figure 16. Comparative analysis of wall stress at several planes along stenotic region of carotid artery. Artery subject to constriction by device D2 (left column) and D3 (right column). D3 induced 16% more wall stress along the plane of view considered in top row, while the same device induced 4% increase in stress (bottom row) further downstream.

Influence of both devices on hemodynamics of the flow domain was comparable. At the stenosis, difference between device induced wall shear stress in both cases was observed to be only 1.4% while peak velocity difference was 2.3%.

5.1.2.3 Discussion

This study elicited the effects of design changes on localized wall stretch and corresponding stresses. Device D3, with pinhole section of the strut retracted outward, enhanced area for fluid flow prior to the entrance of stenotic region. As the device induced stenosis, other

sections of arterial wall compensated for loss in fluid area by undergoing radial expansion. At the entrance of stenosis, facilitated by enhanced flow area due to design changes in D3, arterial wall stretch increased compared to the same region in the artery subject to constriction by D2. Such an increase in wall stretch resulted in an elevation of localized wall stresses by 16%. Similar trend was observed toward the terminal ends of device D3, downstream of stenosis, where the strut retracted outward facilitated increased wall stretch and enhanced wall stress compared to D2 induced stress. FSI results clearly indicated that the devices induced varied localized wall stresses, without significantly affecting flow domain hemodynamics and that even small design changes could influence wall biomechanics at the region of interest.

5.1.3 Case Study 3

With FSI proving that design changes induced elevated localized wall stress and thereby may better activate baroreceptors, the next case study was conducted to evaluate a completely revamped stenotic design in stimulating baroreceptors. This device was to be deployed on subject based carotid models. Thus, as a preliminary evaluation, deployment of this particular device on a simplified carotid model was conducted.

5.1.3.1 Device Configuration

Device D4 was slid onto the carotid wall, similar to setup shown for previous devices D2 and D3.

5.1.3.2 Results & Discussion

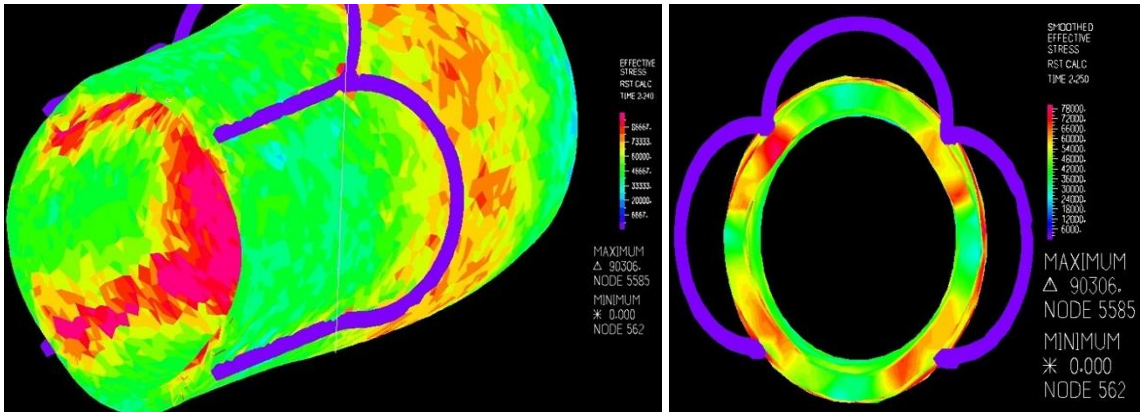

Figure 17. Stress distribution shown on a section of carotid artery fitted with device D4 (left). Peak wall stress, occuring on the inner surface of carotid, was 90 kPa. Front view of cross

section of artery wall with device (right). Regions of elevated wall stresses are indicated by red spots and occur at points of contact with the device.

A cross sectional analysis of the carotid and associated stress distribution showed that the device induced uniformly elevated wall stresses at regions of contact with the arterial wall. Such a device-induced peak stress that developed on inner walls of the carotid was observed to be 90 kPa. The trend of elevated wall stresses at regions of compression by device was in concordance with previously observed trends.

5.1.4 Conclusion

Using FSI methodology, different extravascular stenotic devices were evaluated for mechanical stimulation of baroreceptors. General trend observed in all simulation results indicated that devices induced localized elevation of wall stress, corresponding to wall stretch, at regions of contact with device struts.

Of all devices evaluated, only device D4 was practically convenient for deployment on a physiologic carotid model. Thus, evaluation of device D4 fitted onto subject specific carotid model was conducted, results of which are discussed in the following sections.

5.2 Evaluation of extravascular and endovascular devices on subject based carotid arteries

Previous section elicited the effect of device deployment on simplified carotid models. For a thorough investigation of the effects of device deployment, FSI simulations were conducted of extravascular and endovascular custom devices deployed in subject based carotid models. Following sections pertain to results of these simulations. This comparative study is in accordance with specific aim #1.

5.2.1 Extravascular Device - D4

Device D4 was clamped to sinus of physiologic carotid model CA2 such that the device struts' compression would induce localized wall stretch and thereby activate sinus baroreceptors. Arterial wall was stretched 18% axially and pressurized to 110 mm Hg prior to start of simulation. Boundary conditions applied for fluid domain were inlet pressure ranging between 108/77 mm Hg and outlet parabolic velocity profiles. Average flow rates exiting out of ICA and ECA were 4 ml/s and 3 ml/s respectively, corresponding to which the peak velocities were 22 cm/s and 52 cm/s. Device boundary conditions were radial displacement applied to the vertical struts.

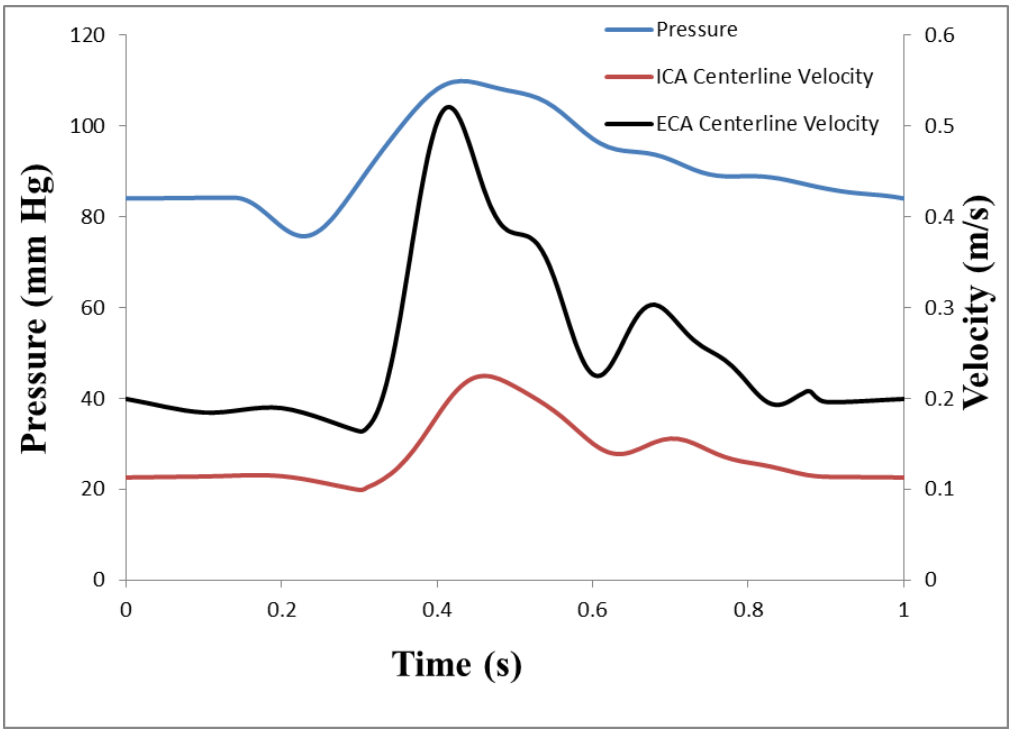

Chart 2. Pressure and velocity boundary conditions applied for the physiologic carotid model CA2

Figure 18. Setup showing device D4 clamped to physiologic carotid model CA2 prior to start of simulation (left). Post simulation, image on right, shows carotid wall subjected to 18% axial stretching and device struts constricting arterial wall radially.

5.2.1.1 Results

FSI predicted elevated wall stresses of approximately 371 kPa in the bifurcation region, close to entrance of ECA branch, with regions of substantially high stresses along CCA branch as well. However, to observe the effect of device at the clinically consequential region of ICA sinus, cross-sectional analysis of stress distribution downstream of bifurcation was conducted, the results of which are presented in Fig 20.

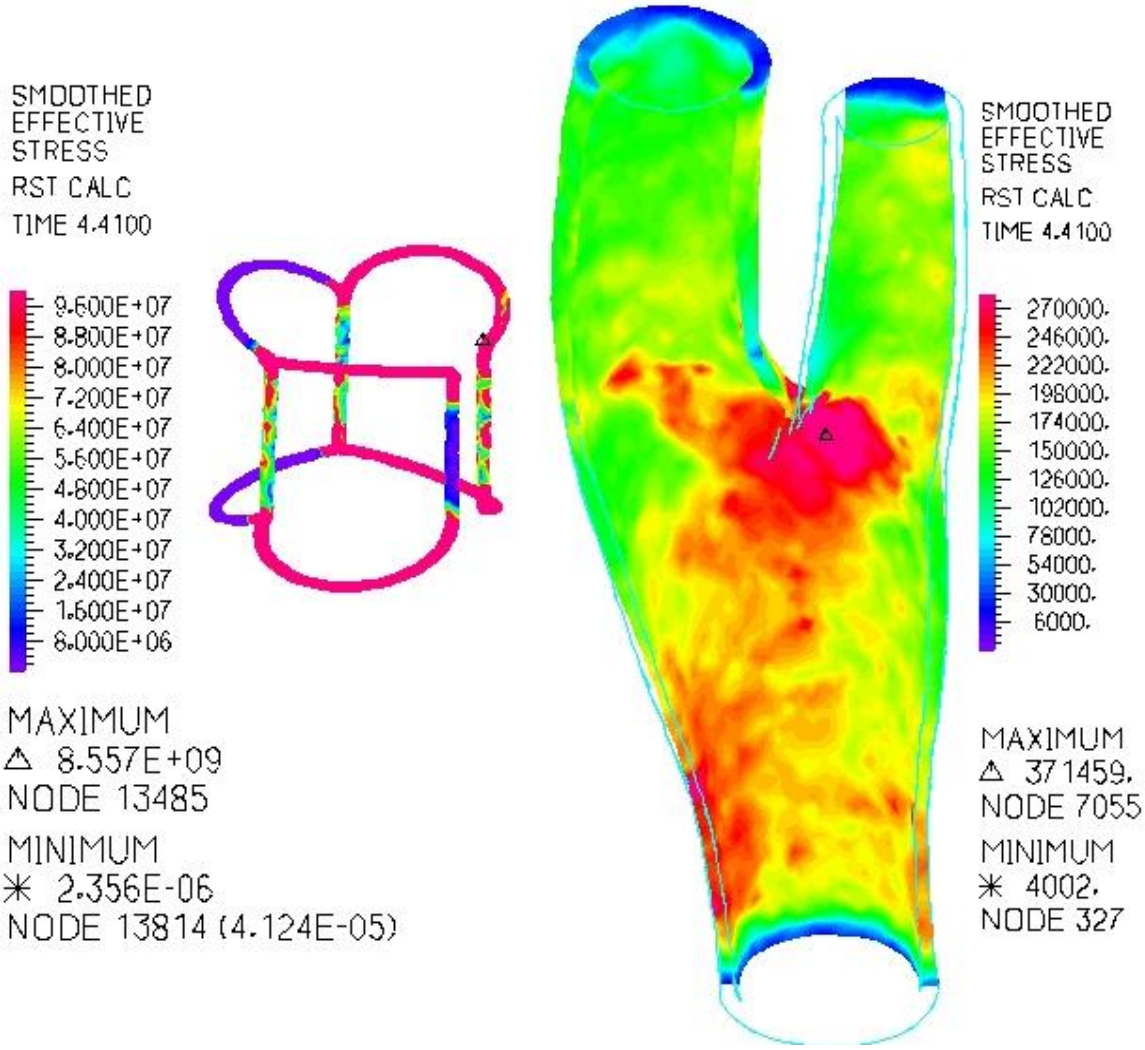

Figure 19. Stress distribution on device (left) and on the overall model of carotid artery (right) are shown. Device deployment on ICA sinus induced localized elevation of wall stress. However, when the overall carotid model was considered, peak stress of 371 kPa occurred at the bifurcation.

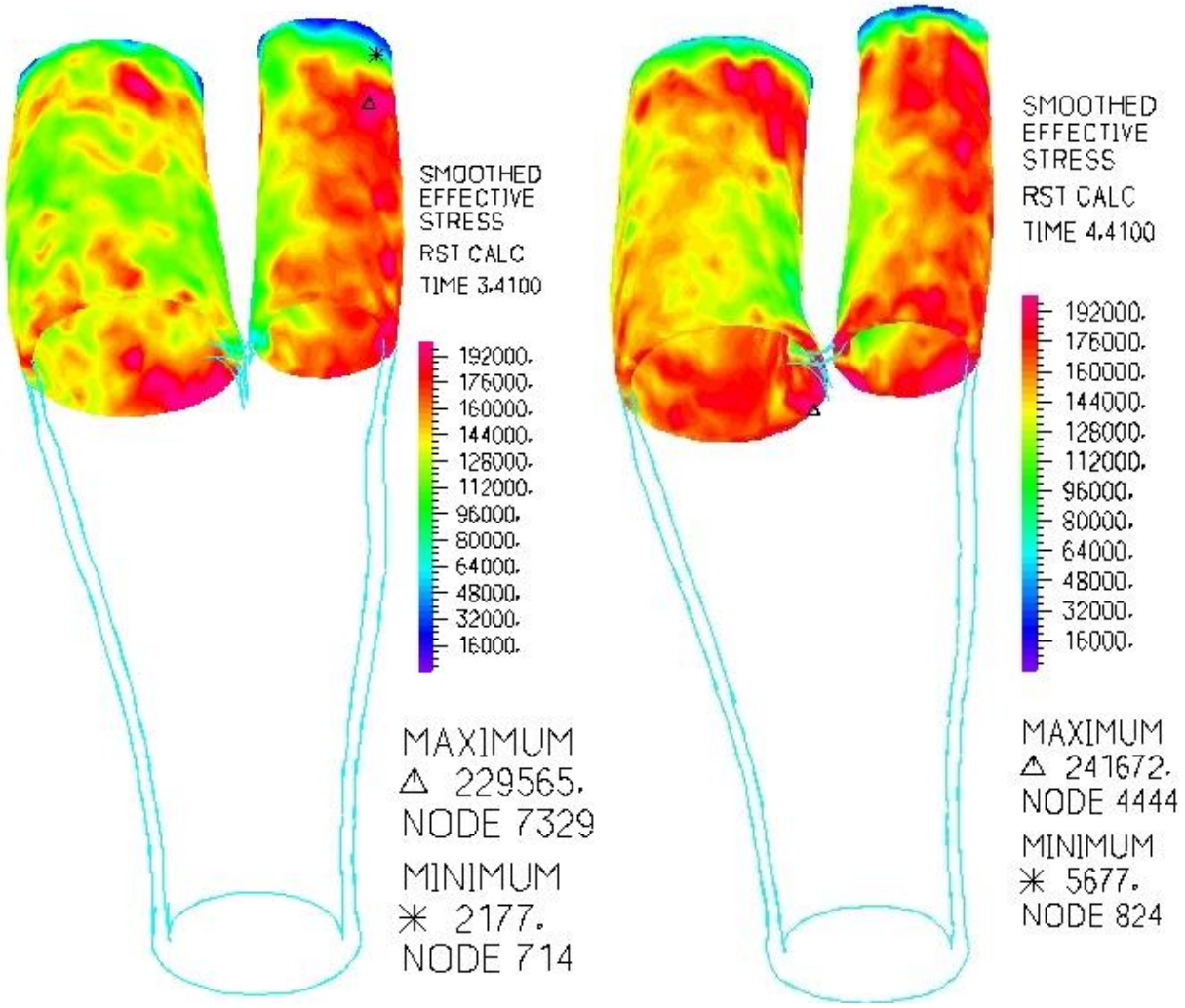

Figure 20. Comparison of wall stress in the sinus of carotid for the case without device (left) and with device deployed (right). Peak wall stress due to device deployment at the sinus was observed to be 242 kPa, while inherent stress in sinus of carotid without any stenotic devices attached was approximately 198 kPa.

For the control case of carotid without any device, FSI predicted sinus wall stresses in the range of 198 kPa at systole and under normotensive conditions. A stenotic device constricting the sinus was observed to induce localized wall stretching, thereby elevating wall stress to 242 kPa, which was a 22% increase in stress at baroreceptor region. However, since circumferential and longitudinal arterial wall stretches are the biomechanical parameters that instigate baroreceptors [72], a comparative analysis of wall stretches of carotid sinus, in cases with and without devices, was conducted. Accordingly, simulations predicted 7% decrease in

circumferential stretch, 1.8% increase in longitudinal stretch and 3% increase in von Mises equivalent stretch, at the sinus region due to stent deployment. In order to evaluate the effect of device deployment on the entire carotid, a comparative analysis of stress distribution on the overall model of carotid was conducted, as shown in Fig 21. Analysis revealed that the device induced a 7% increase in inherent bifurcation peak stress.

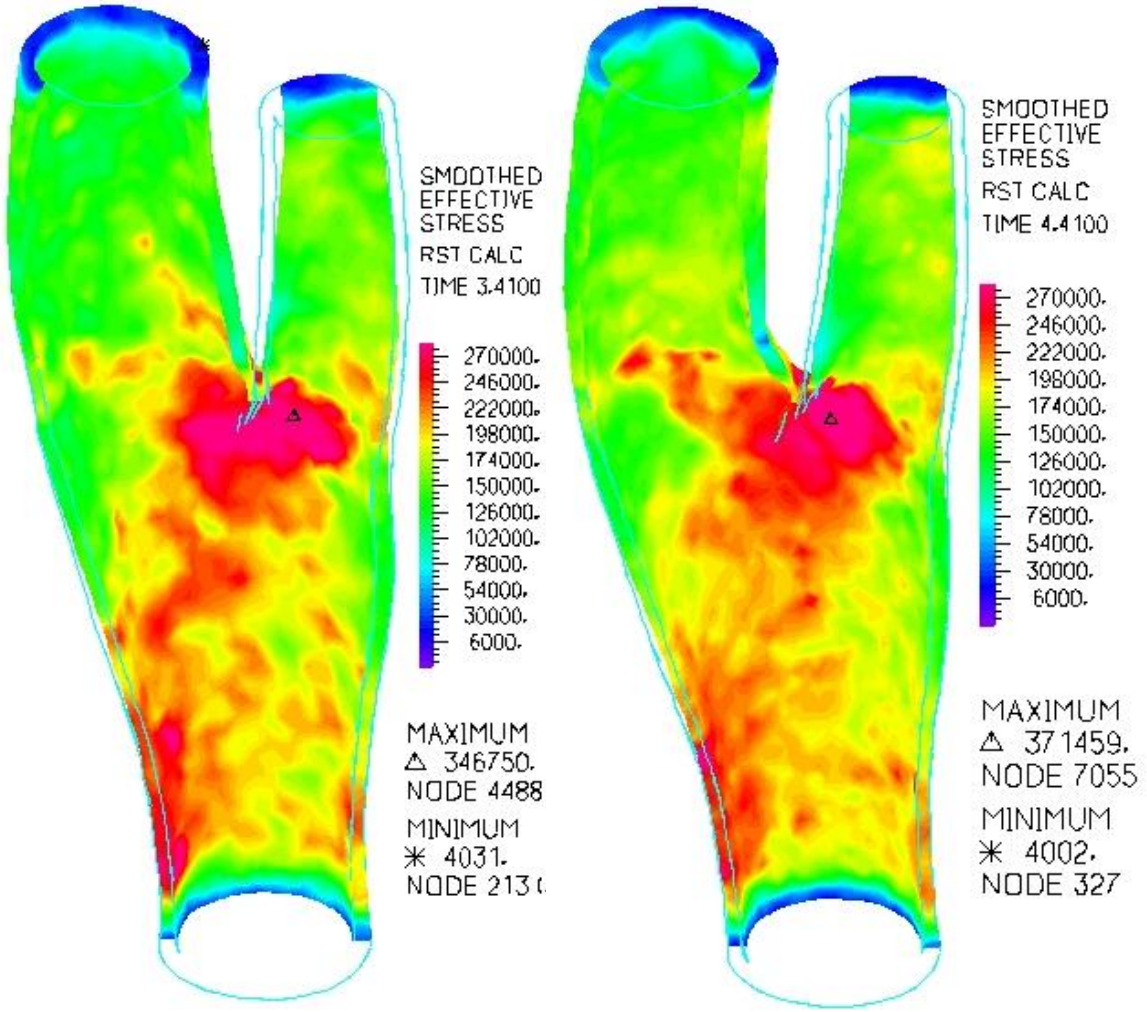

Figure 21. Comparison of wall stress in the overall model of carotid for the case without device (left) and with device deployed (right). Peak wall stress at bifurcation was observed to increase 7% from 347 kPa to 371 kPa due to device deployment at the sinus.

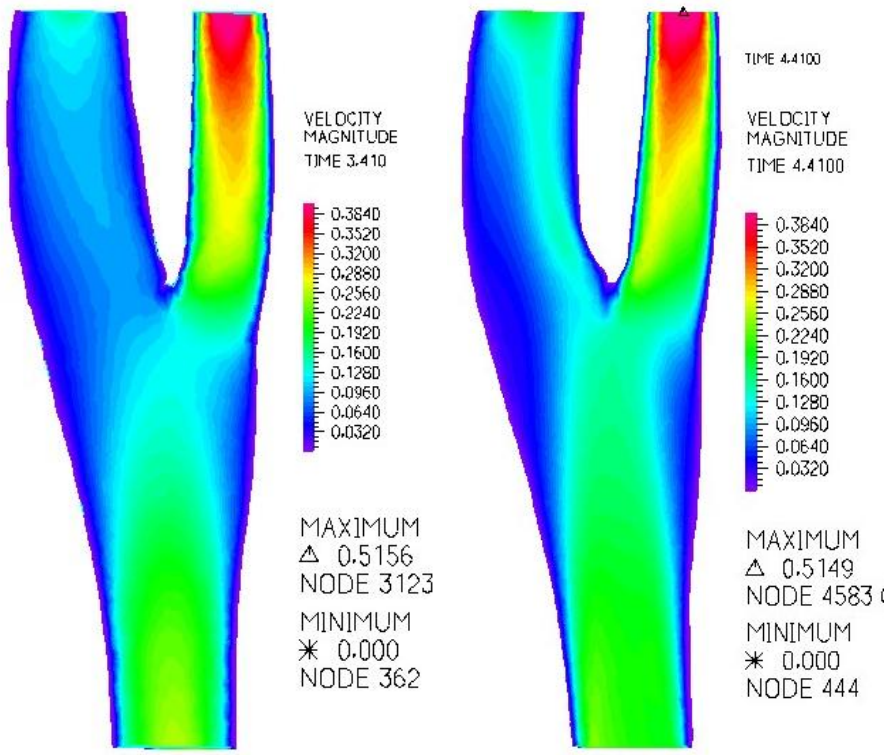

Figure 22. Velocity contour plots, shown at systole, for carotid without device (left) and with device deployed (right). Systolic peak velocities in ICA and ECA, for both control and device case, were 22 cm/s and 52 cm/s respectively. Device deployment enhanced flow separation at the sinus, without influencing flow magnitude.

Simulation results facilitated prediction of consequential hemodynamic parameters, such as velocity and wall shear stress, and influence of device deployment on them. A comparison of velocity contour of carotid lumen for the case with and without device revealed that the device did not hamper velocity magnitudes, as in both cases, exit velocities from ICA and ECA branches at systole were 22 cm/s and 52 cm/s respectively. However, device deployment on ICA branch induced flow separation at the sinus, as seen in Fig 22. No adverse effects on flow profile in other branches were observed. To observe development of flow separation at sinus, a time progressive series of images depicting velocity contours at various points along the cardiac cycle are presented in Fig 23. At diastole, prominent recirculation zones were observed at the carotid sinus section and along inner walls of CCA proximal to entrance of ECA branch.

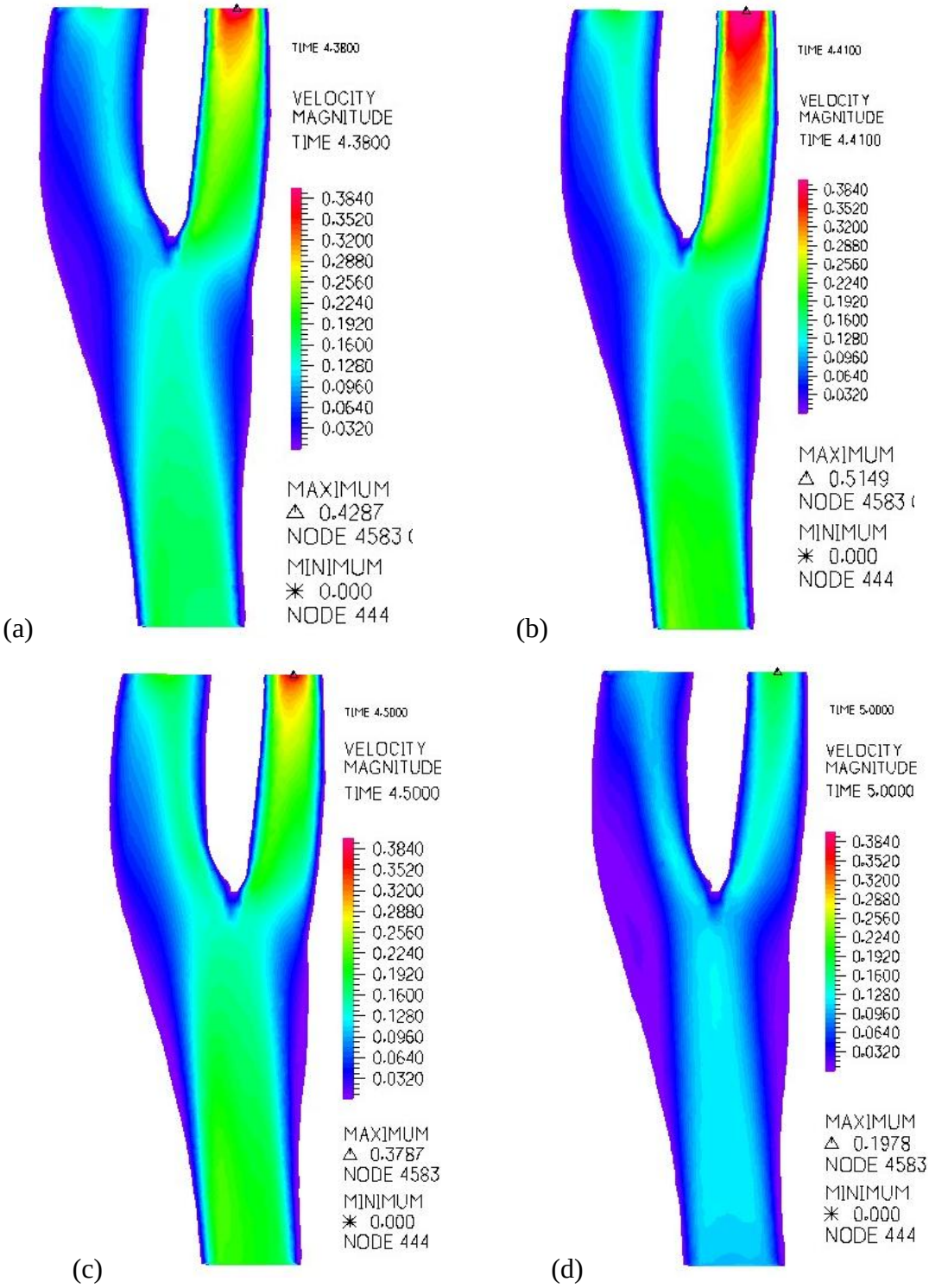

Figure 23. Shown in the order of (a)-(b)-(c)-(d) are velocity contour plots at pre-systole, systole, post systole and late diastole. Systolic peak velocities (b) at ICA and ECA exits were 22 cm/s and 52 cm/s respectively. At diastole (d), prominent recirculation zones were observed at ICA-CCA juncture, coinciding with sinus, and also along inner wall of CCA prior to ECA branch.

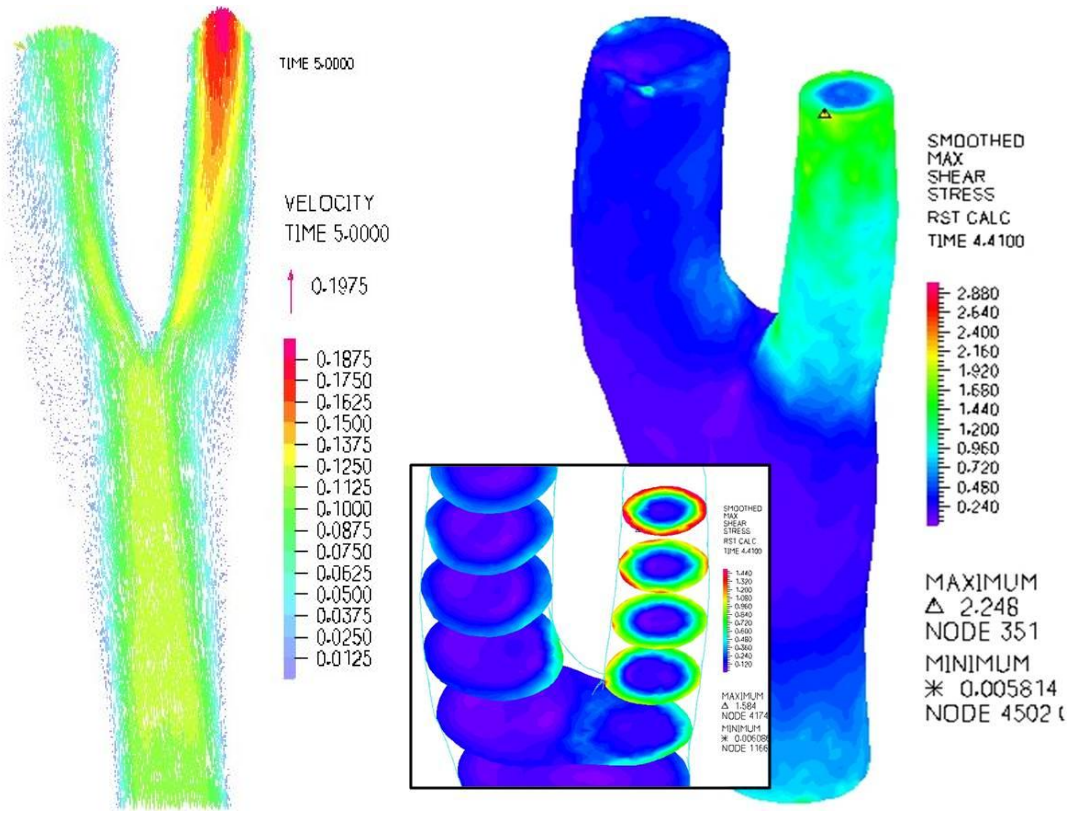

Figure 24. Velocity vector plot (left) is shown at diastole and wall shear stress contour (right) is shown at systole. Inset shows WSS in the sinus region. Velocity vector analysis showed recirculation zones at the sinus and in CCA prior to entering ECA branch. WSS in sinus was observed to be in the range of 1-3 dyn/cm^2 while it was 2-5 dyn/cm^2 in CCA, approximately 10 dyn/cm^2 in ECA and 1-2 dyn/cm^2 at the recirculation zones.

A combined analysis of velocity vector and wall shear stress distribution, as shown in Fig 24, revealed a prominent recirculation zone in the sinus which extended proximal and distal to the sinus as well. This region was observed to have typical low WSS values in the range of 1-2 dyn/cm^2. Device deployment did not have any apparent effect on the overall sinus WSS which was observed to be in the range of 1-3 dyn/cm^2 irrespective of presence or absence of device. Narrow flow area coupled with high velocity in ECA branch resulted in a higher WSS of approximately 10 dyn/cm^2.

5.2.2 Endovascular Devices

All devices evaluated thus far constricted carotid artery from outside the vessel wall. To explore alternative and efficient methods of mechanical stimulation of baroreceptors, endovascular stents were designed to stretch the sinus intra-luminally. For a holistic evaluation of the efficacy of such stents in activating baroreceptors and any adverse effects that such stents may have on associated hemodynamics, FSI analysis was conducted on the three interacting bodies - artery wall, blood flowing through it and the deployed endovascular stent. Two separate stent designs, custom made for two carotid models, were evaluated as separate case studies.

5.2.2.1 Case Study 1 - Stent design D5 deployed in physiologic carotid model CA2

A crimped design of stent D5 was deployed in the carotid sinus such that the stent expansion would induce localized increase in sinus wall stretch and thereby activate baroreceptors located there. Stent D5 was custom made for the physiologic carotid model CA2 such that the fully expanded stent would have a diameter more than the systolic inner diameter of carotid sinus. Boundary conditions for fluid domain were the same as that applied for the extravascular device case. Stent boundary conditions were radial displacement, defined relative to the centroid of stent, and applied to the stent's vertical struts. Radial displacement boundary conditions were applied such that the expanded stent diameter would be 20% more than systolic inner diameter of sinus of the control. Carotid artery was stretched to the same 18% of its axial length, as had been done for the extravascular device case.

Figure 25. Setup showing stent D5 placed in the sinus of physiologic carotid model CA2 prior to start of simulation (left). Post simulation, image on right, shows carotid wall subjected to 18% axial stretching and stent fully expanded.

5.2.2.1.1 Results

Endovascular stent D5 deployed in the sinus was observed to enhance localized wall stresses at sinus region, from 198 kPa in the control case (carotid without stent) to 305 kPa, which was a 54% increase in stress at baroreceptor region. Comparative analysis is presented in Fig 26. This increase in sinus stress value corresponded to a 2.5% increase in circumferential stretch, 7.5% increase in longitudinal stretch and 6% increase in von Mises equivalent stretch. Since the stent was observed to induce better increase in both circumferential and longitudinal wall stretches compared to extravascular device, in depth analysis of several important biomechanical parameters were conducted, as discussed below.

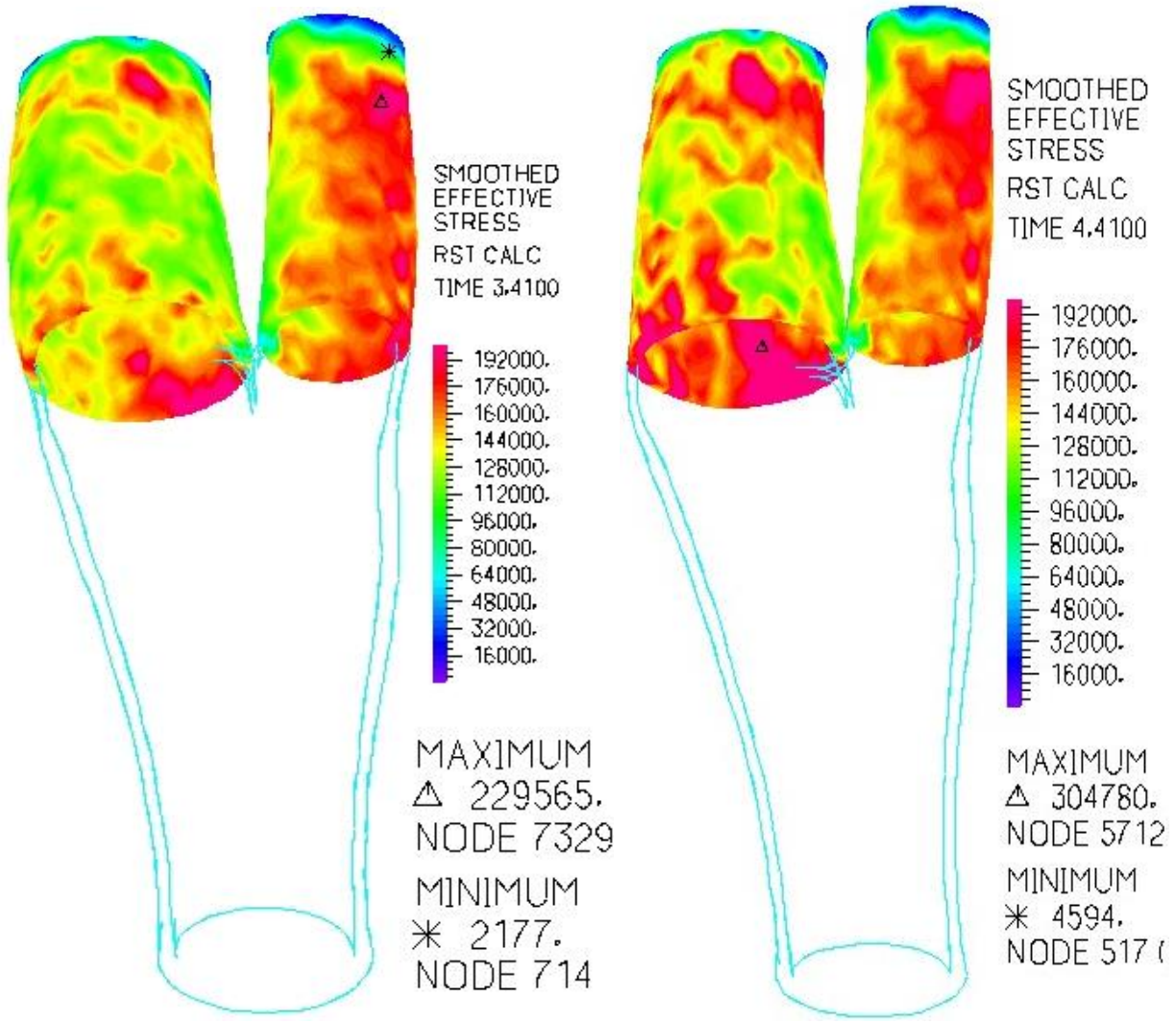

Figure 26. Comparison of wall stress in the sinus of carotid without stent (left) and with stent deployed (right). Peak wall stress due to stent deployment at the sinus was observed to be 305 kPa, while inherent stress in sinus of carotid without any implants was approximately 198 kPa.

Apart from predicting localized elevation of wall stresses, simulation predicted a decrease in arterial wall compliance by 22% due to stent deployment. Furthermore, the stent was observed to induce a significant pulsating wall stretch effect at sinus region, a snapshot of which is shown in Fig 27.

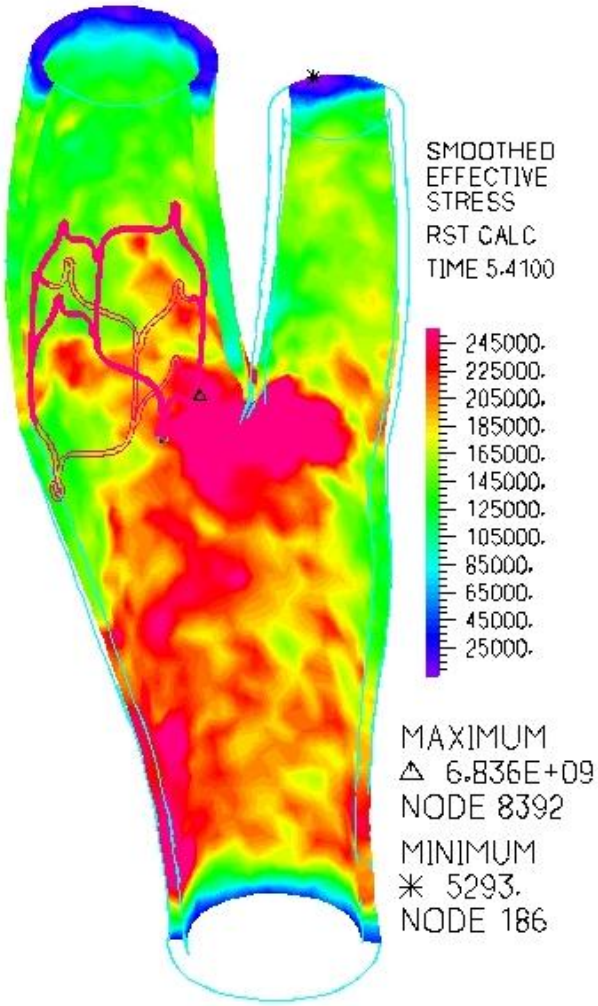

Figure 27. Cross section of wall stress distribution shown on the inner walls of carotid artery and fully expanded stent.

As further substantiation and for better visual confirmation, a plot of sinus wall stretch over an entire cardiac cycle, as presented in Fig 28, revealed wall pulsatility for the control carotid sinus to be in sync with cardiac cycle. However, sinus of device deployed carotid was observed to have a lower wall stretch pulsatility compared to control. A more detailed analysis of time variance of wall stretch, at the section of carotid sinus between struts of the stents, is shown in Fig 29. This analysis indicated that between the stent struts, arterial wall had a more pronounced pulsatility compared to the analysis presented in Fig 28. Such a pulsating effect may ensure baroreceptors do not adapt to the mitigative effects that the device would have on hypertension.

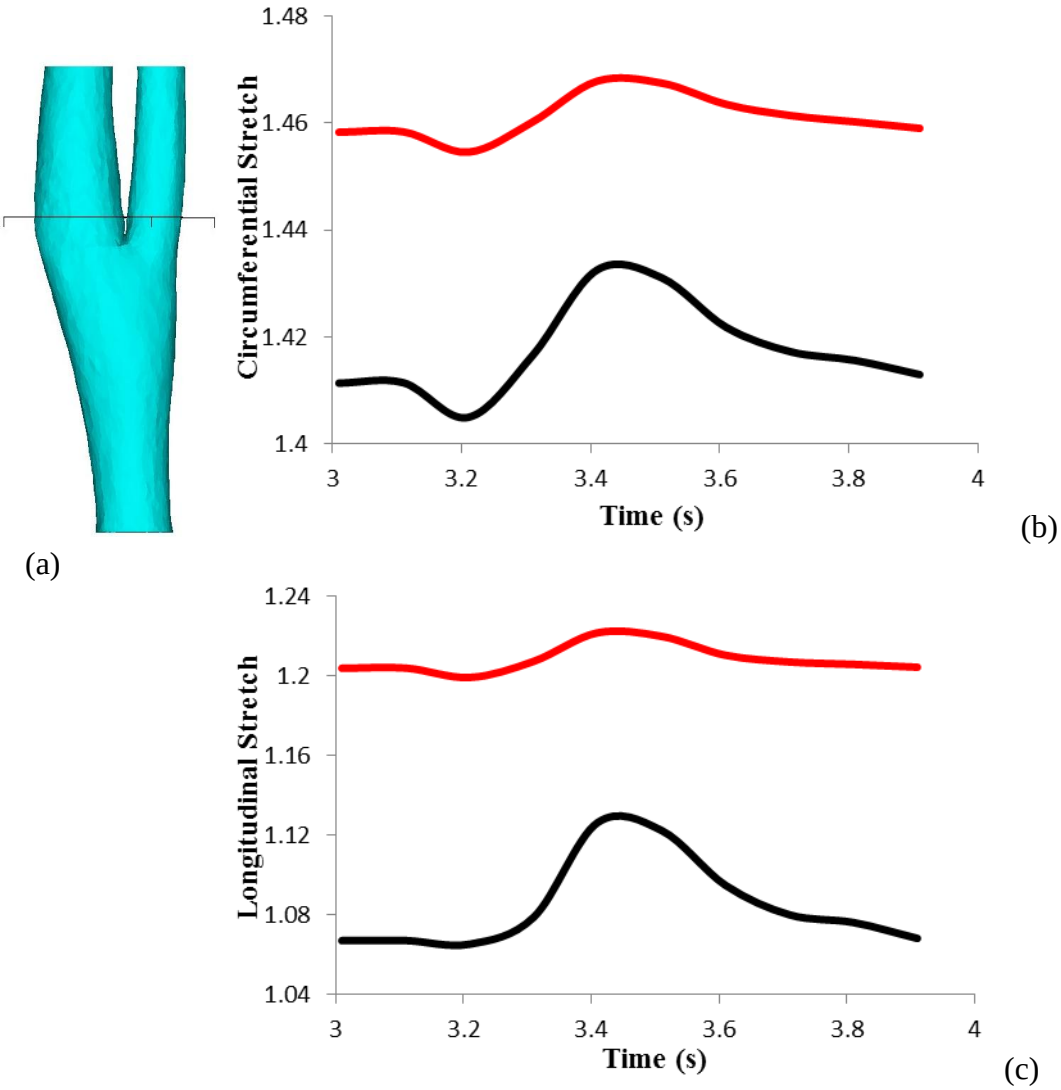

Figure 28. Section of carotid sinus, at the plane shown in (a), is chosen for analysis of time variance of wall stretch. Circumferential and longitudinal wall stretch variance with time are presented in (b) and (c). Wall stretch for control case is indicated in black while that for carotid with device is in red. Control case had wall stretch pulsatility in synchroneity with pulsatility of blood flow. Device deployed carotid had dampened wall stretch pulsatility.

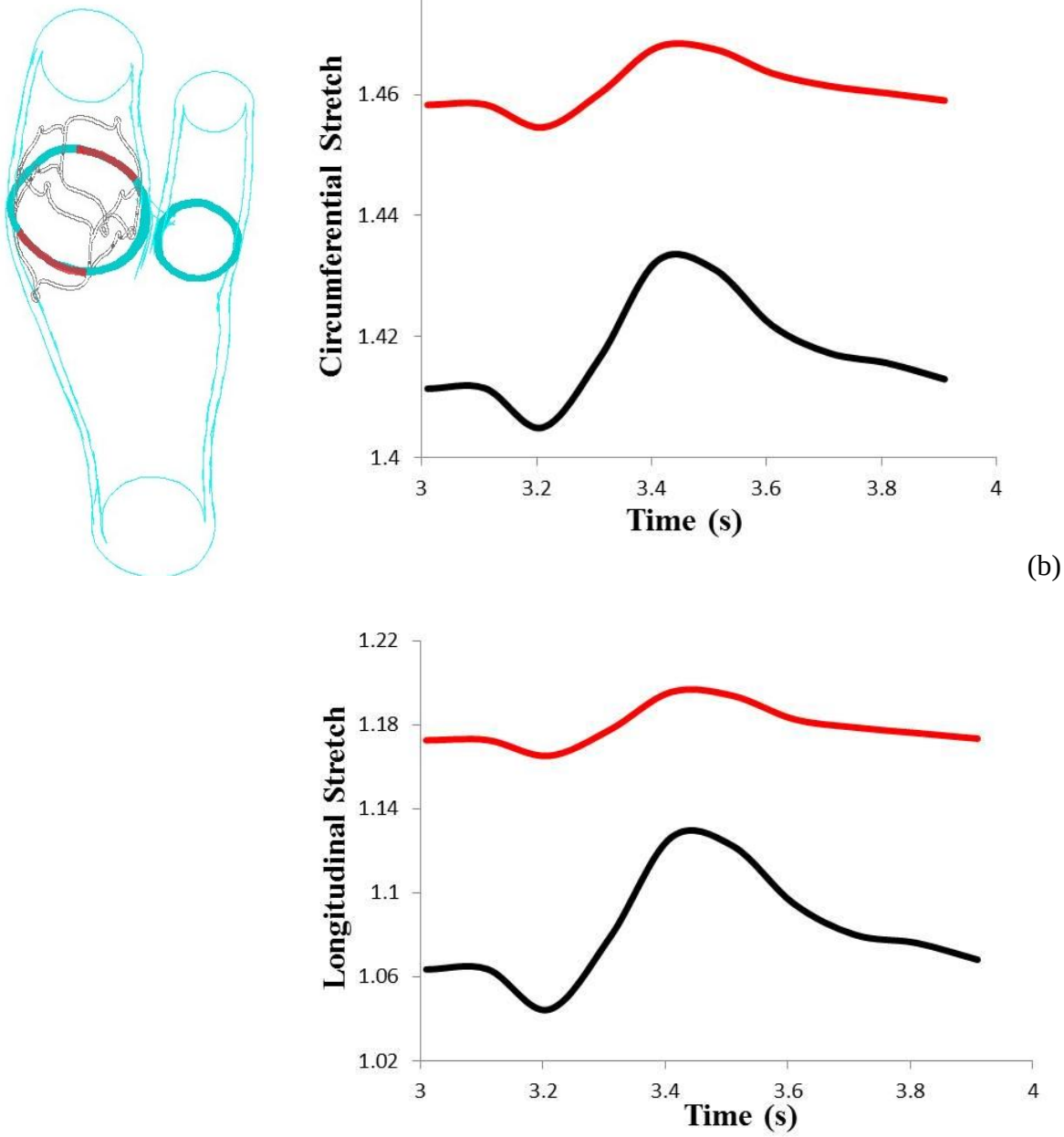

Figure 29. Section of sinus wall between stent struts, shown in (a) and indicated in red, is chosen for time variance wall stretch plots. Circumferential and longitudinal wall stretch variance with time are presented in (b) and (c). Wall stretch for control case is indicated in black while that for carotid with device is in red. The section of sinus wall between struts had more pronounced pulsatility compared to device deployed carotid pulsatility shown in Fig 28.

Predicted stress values may be influenced by several factors such as location and orientation of stent deployment, diameter of fully expanded stent, dimensions of carotid artery and associated boundary conditions. Since the employed carotid models were subject specific and applied boundary conditions pertained to normotensive values observed in individuals, only the influence of stent orientation and extent of stent expansion on arterial wall stresses were evaluated as separate cases.

5.2.2.1.1.1 Influence of stent orientation angles on wall stress

To evaluate the effect of varying stent orientations, simulations were conducted with stent deployed in different angles relative to the ICA axis. Stent location was not altered since the objective was to deploy the stent at sinus and not elsewhere. A maximum axial rotation of 8 degrees relative to ICA axis, which significantly altered stent orientation compared to other angles as shown in Fig 30, was observed to evoke only a 0.2% drop in wall stress values at the sinus.

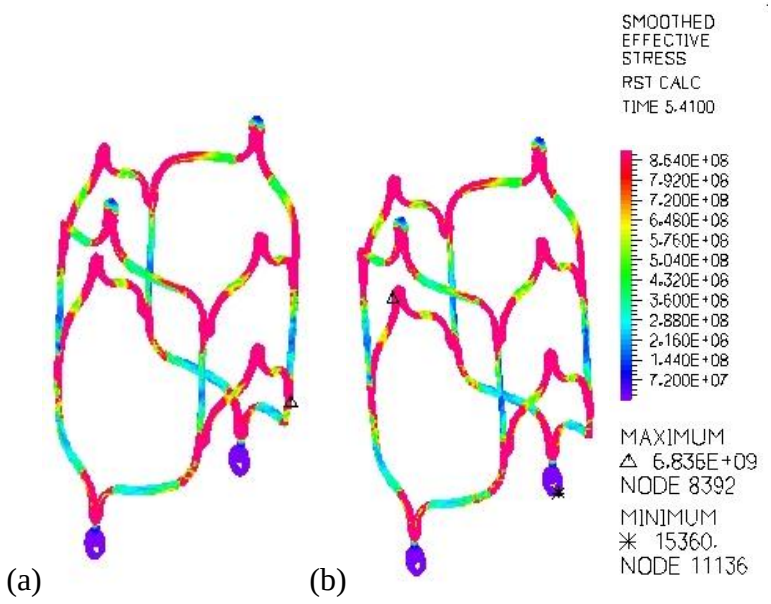

(a) (b)

Figure 30. Comparison of wall stress distribution on stent model when its orientation is changed by an 8 degree axial rotation (b) compared to initial deployment angle (a). No consequential changes were observed in stress magnitude or distribution in both stent and carotid models.

5.2.2.1.1.2 Stent diameter and its relation to wall stress

To evaluate the effect of stent expansion on arterial wall stresses, simulations were conducted with stent expanded to a range of diameters lesser and more than the systolic sinus inner diameter (9.27 mm).

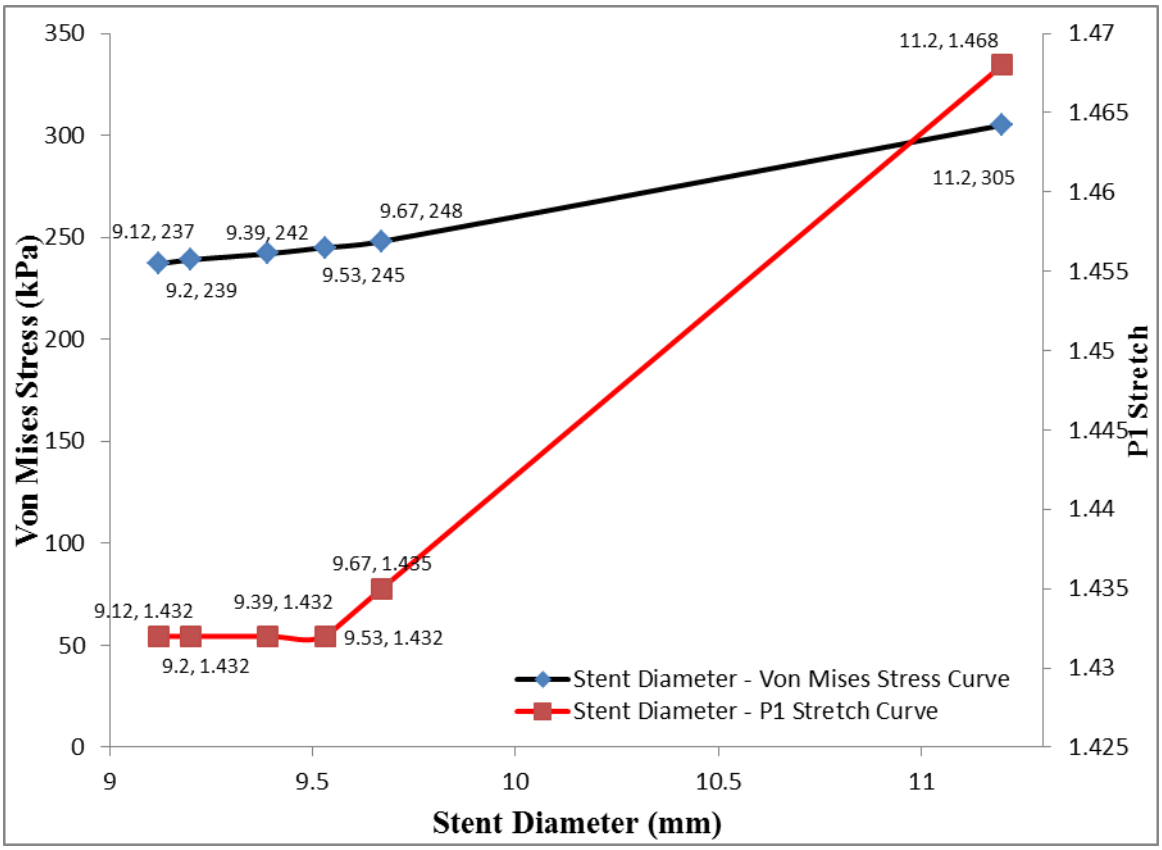

Chart 3. Variation of wall stress and principal circumferential stretch with stent diameter for carotid model CA2

Results indicated that as the stent diameter increased, wall stresses increased. Changes in wall stretch were trivial for the range of stent diameters 9.12-9.53 mm after which it increased. Previous studies had indicated that oversizing the unloaded diameter of stents by 20% more than vessel wall diameter provided sufficient fixation force within blood vessels to prevent migration of the stent post-deployment [73]. To evaluate wall biomechanics at a stent diameter that was 20% more than systolic sinus inner diameter, simulation was conducted with stent expanded to 11.2mm, for which the stretch and stress results have already been presented earlier and which

correlate well with the results of Chart 3. The MAP of normotensive case simulated was 87 mm Hg which is close to the MAP at which baroreceptor sensitivity is maximal (95 mm Hg) as mentioned earlier. Thus, at 87 mm Hg MAP, any amount of wall stretch would induce baroreceptors to fire action potentials. Less than 5% difference in wall stress values was observed between stent diameters of 9.12mm and 9.67mm, and 0.2% difference in wall stretch values for the same stent diameter range. The prime objective while designing stents for use in hypertension treatment therapy is to activate baroreceptors with least adverse effects due to deployment as possible which also includes inducing low wall stress values. Thus, for the considered physiologic carotid model and stent design, stent manufactured to expand to 9.12mm would activate baroreceptors with least amount of induced wall stress. However, for the stent to be anchored in its place of deployment, the expanded stent's diameter should be more than 20% of the systolic sinus inner diameter. Thus, the entire study and analyses have been conducted for the stent case which has an expanded diameter 20% more than sinus diameter.

5.2.2.1.1.3 Influence of stent deployment on overall wall stress

As baroreceptors are located in the sinus and endovascular stents are deployed at that location, evaluation of stent's efficacy in stimulating baroreceptors required attention primarily in the sinus region. However when the entire carotid model was considered as shown in Fig 31, invariably in both models, peak stress occurred close to the bifurcation and at the entrance of ECA. Location for such peak stress in the overall model was irrespective of presence or absence of any implant. Stent was not observed to induce any adverse effects on the wall biomechanics as deployment in the sinus region induced only a 0.6% increase in bifurcation peak stress (which is the overall peak wall stress) from 347 kPa to 349 kPa. As peak stress at bifurcation does not influence hypertension treatment therapy, it was not considered in stress analyses.

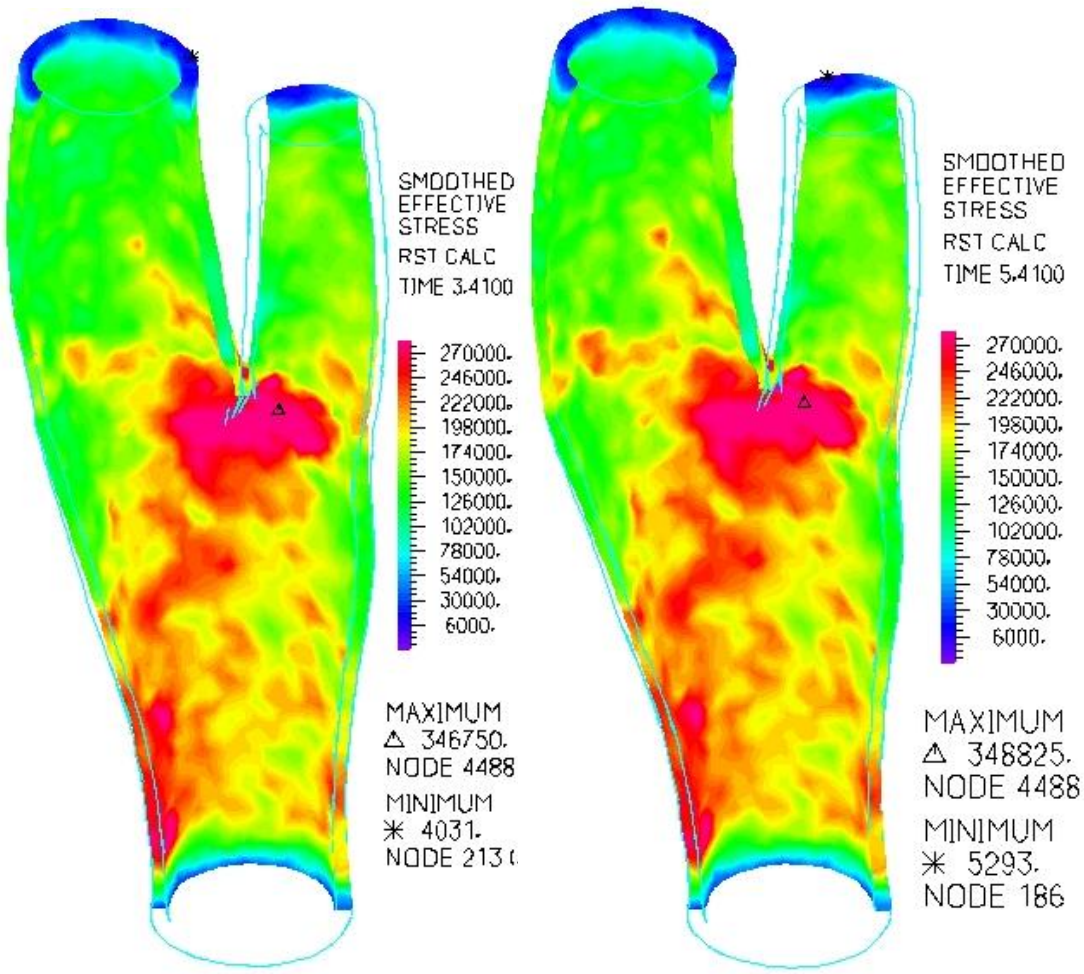

Figure 31. Wall stress distribution in the overall model of carotid artery without stent (left) and with stent deployed (right). Peak stress occurring at the bifurcation in stent deployed case was observed to be 349 kPa while inherent stress in the bifurcation of the control was 347 kPa.

5.2.2.1.1.4 Analysis of hemodynamic parameters

Peak velocities of 22 cm/s and 52 cm/s were observed in ICA and ECA respectively, for both control and stent deployed cases. As shown in Fig 32, stent deployment increased sinus area thereby enhancing flow separation that was inherent for such a physiologic carotid model. Stent deployment however had no apparent effect on the flow profile in other branches of the carotid.

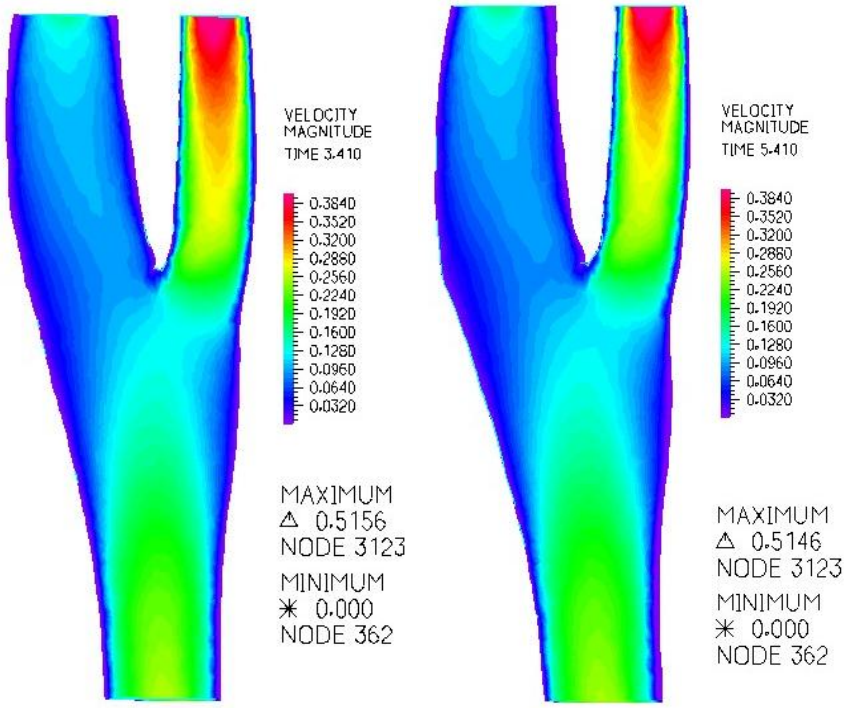

Figure 32. Velocity contour plots, shown at systole, for carotid without stent (left) and for stent deployed case (right). Systolic peak velocities in ICA and ECA, in both control and stent case, were 22 cm/s and 52 cm/s respectively. Stent deployment increased sinus area thereby enhancing flow separation at the sinus.

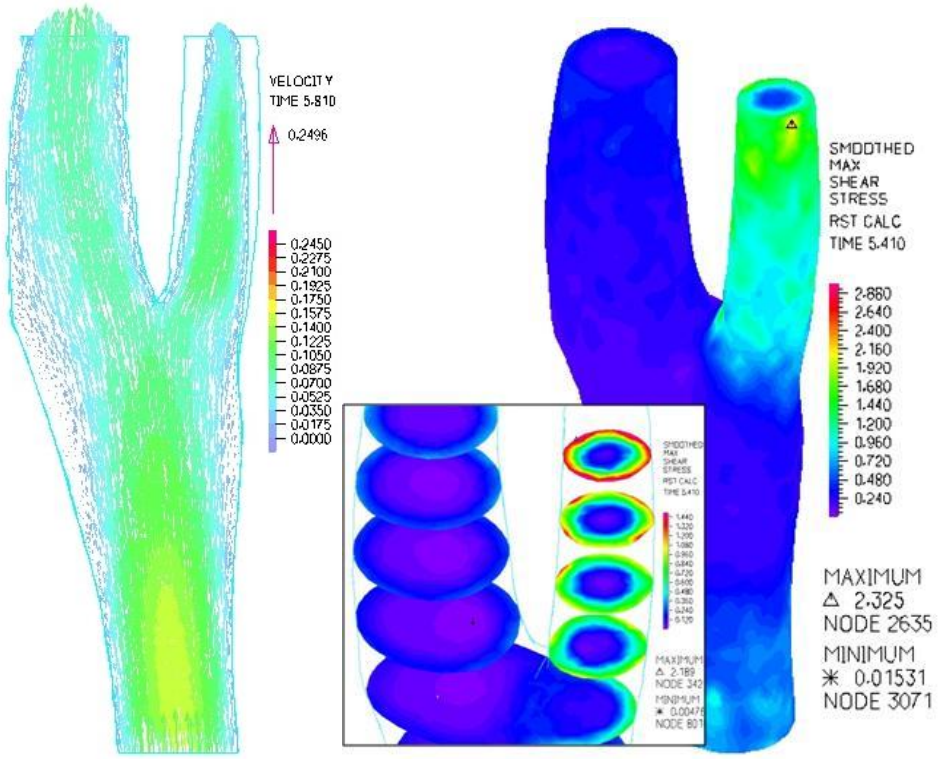

Figure 33. Velocity vector plot (left) shown for early diastole and wall shear stress contour (right) shown for peak systole of first carotid model. Inset shows WSS in the sinus region. Velocity vector analysis shows recirculation zones close to the wall and at the ICA-CCA junction. WSS in the sinus was observed to be in the range of 1-3 dyn/cm^2 while it was 2-5 dyn/cm^2 in CCA and ICA branches, 10-14 dyn/cm^2 in ECA and 1-2 dyn/cm^2 at the recirculation zones.

Recirculation zones, typical of physiologic carotids, were observed in CCA, close to bifurcation and extending into the carotid sinus. Simulations indicated that these recirculation zones were enhanced slightly by stent deployment and that typical low wall shear stress values, in the range of 1-2 dyn/cm^2, were prevalent in such regions, irrespective of presence or absence of device. Stent also did not affect the overall sinus WSS distribution, which was observed to be approximately 1-3 dyn/cm^2.

5.2.2.2 Case Study 2 - Stent design D6 deployed in diminutive carotid model CA3

Similar to the previous stent case study, a crimped design of stent D6 was deployed at the sinus of carotid CA3. This case study was conducted as per requirements of specific aim #2. For this diminutive carotid model CA3, referenced flow rates [67] were adjusted to 2.05 ml/s and 1.48 ml/s in ICA and ECA branches such that the flow rates would be consistent with the small carotid dimensions and that the wall shear stress (WSS) that develop in these branches would be 20 dyn/cm^2 and 80 dyn/cm^2 respectively. Correspondingly, the applied peak systolic boundary condition velocities were 56 cm/s and 130 cm/s at the outlet of the two branches. However, as the flow rates used for this carotid were non-physiologic, a separate case study was conducted to test the hemodynamic parameters that develop when physiologic flow rates are used, albeit applying such flow rates to a smaller than typical physiologic carotid model may generate non-physiologic elevated hemodynamic values. For such a study, flow rates were doubled to 4.1 ml/s and 2.96 ml/s in ICA and ECA respectively, corresponding to which the applied systolic velocities at the outlets increased to 110 cm/s and 262 cm/s respectively. Applied inlet pressure boundary condition was not adjusted in any of these cases. Carotid artery, in this case study, was stretched to 12% its axial length.

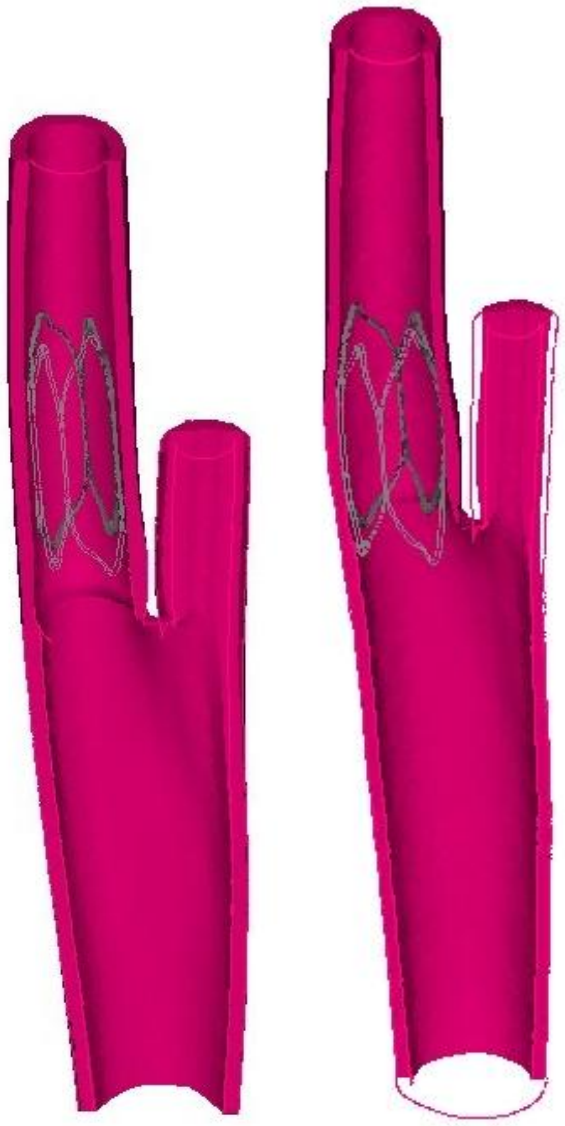

Figure 34. Cross section of carotid artery CA3 with crimped endovascular stent device D6 deployed in ICA.

5.2.2.2.1 Results

A trend in elevation of wall stretch and stress values, due to stent deployment, quite similar to the previous case study, is observed in the diminutive model as well. The custom stent design D6 induced an increase of 6% in both circumferential and longitudinal wall stretches, along with a 54% increase in von Mises equivalent stretch at sinus. Correspondingly, a 50% increase in localized wall stress was predicted, as shown in Fig 35. However, the stent also adversely increased bifurcation wall stress from 211 kPa, in control, to 611 kPa. Significant

variations in these solid domain results were not observed when applied flow rates were varied. For this diminutive model, wall compliance decreased by 17% when stent was deployed at the sinus.

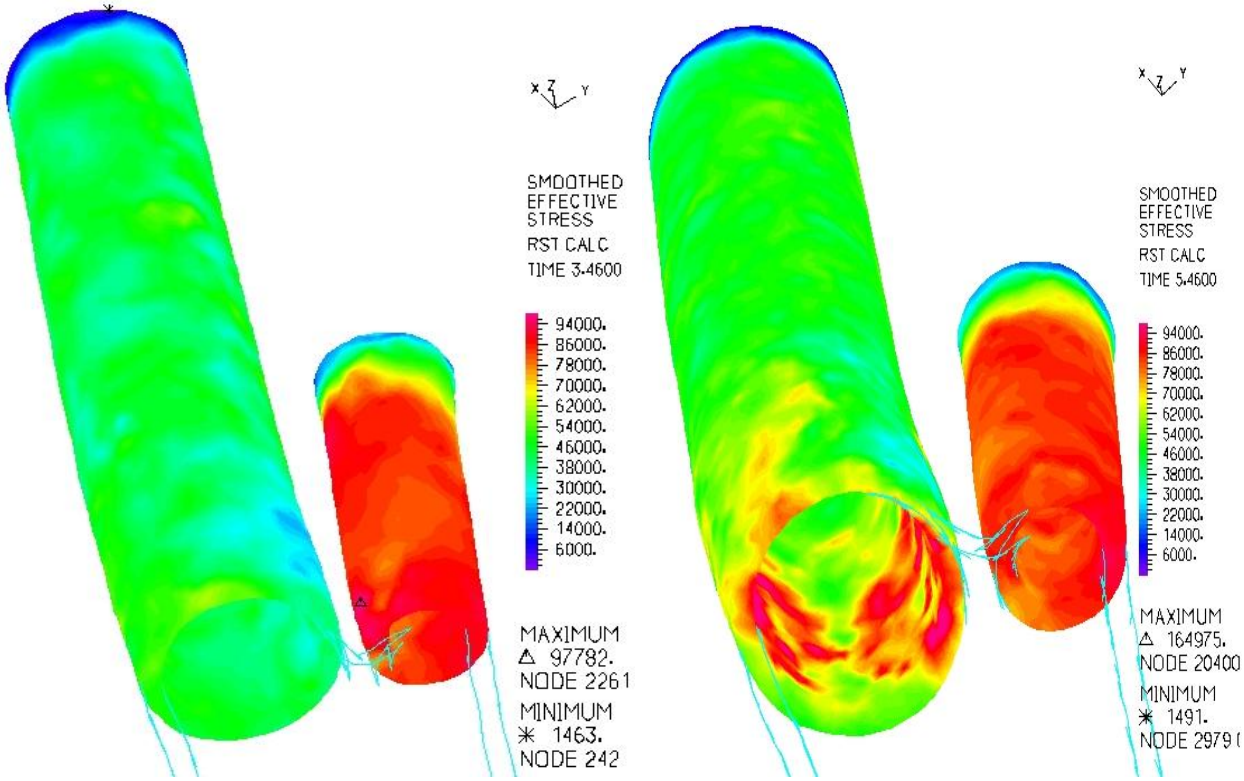

Figure 35. Comparison of wall stress in the sinus of second carotid without stent (left) and with stent deployed (right). Peak wall stress due to stent deployment at the sinus was observed to be 90 kPa, while inherent stress value in ICA of carotid without implants was approximately 60 kPa.

Quite similar to the pulsating effect of stent D5 on the physiologic carotid model, stent D6 was also observed to induce pulsating wall stretch on the carotid wall, as shown in Figs 35 and 36. However, wall stretch pulsatility of this diminutive model was attenuated in comparison to the physiologic model.

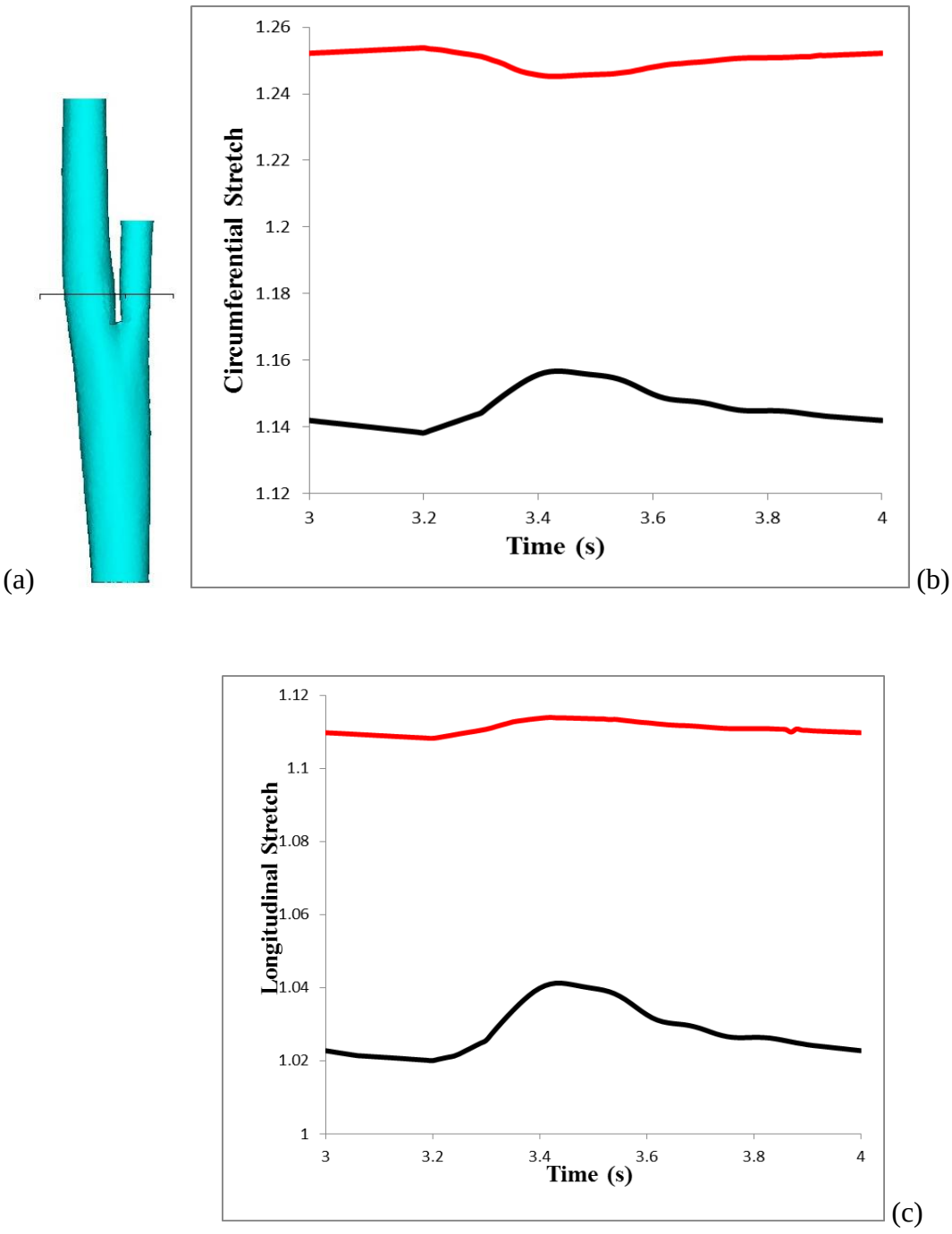

Figure 36. Section of carotid sinus, at the plane shown in (a), is chosen for analysis of time variance of wall stretch. Circumferential and longitudinal wall stretch variance with time are presented in (b) and (c). Wall stretch for control case is indicated in black while that for carotid with device is in red. Control case had wall stretch pulsatility in synchroneity with pulsatility of blood flow. Device deployed carotid had dampened wall stretch pulsatility.

(a)

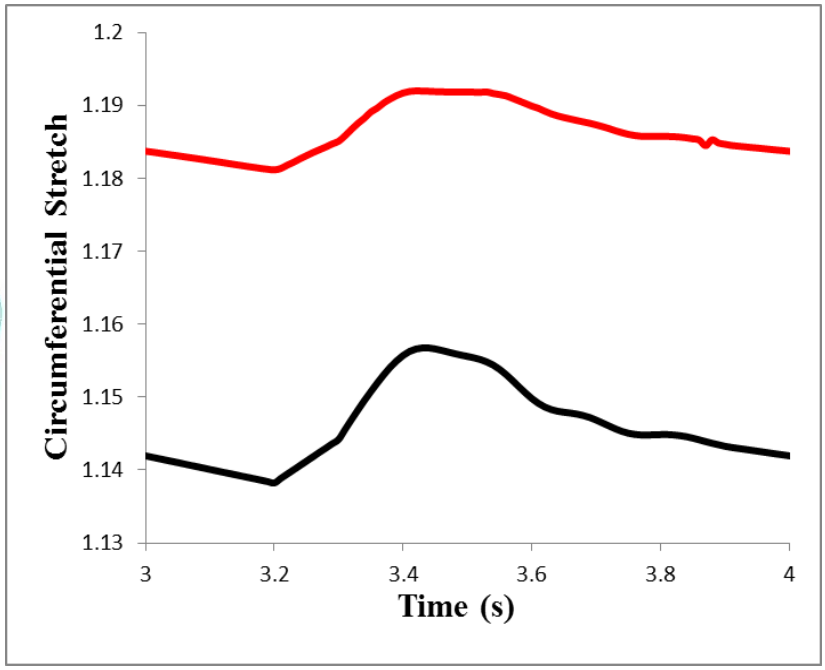

(b)

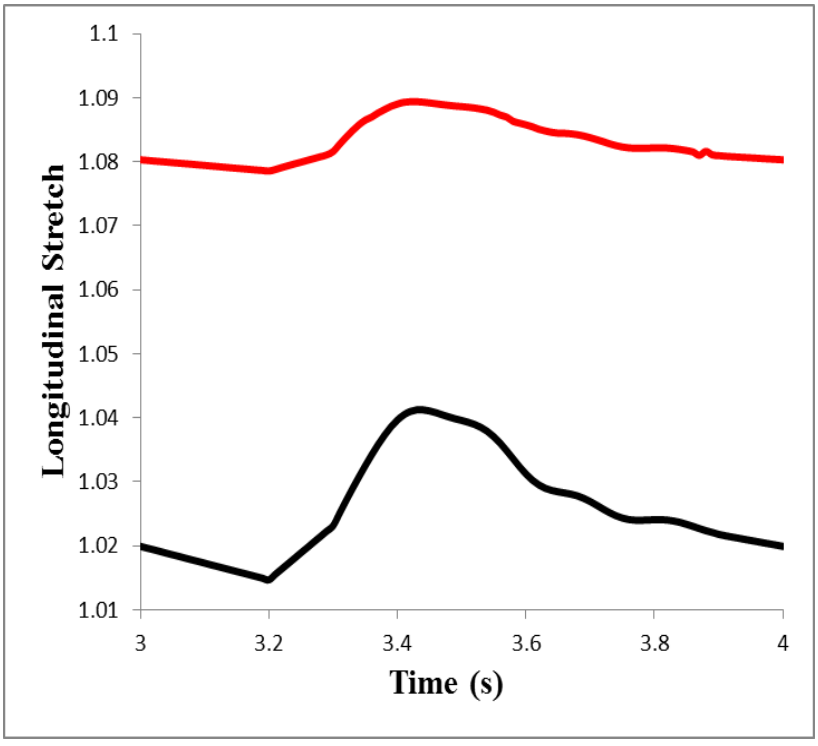

(c)

Figure 37. Section of sinus wall between stent struts, shown in (a) and indicated in red, is chosen for time variance wall stretch plots. Circumferential and longitudinal wall stretch variance with time are presented in (b) and (c). Wall stretch for control case is indicated in black while that for

carotid with device is in red. The section of sinus wall between struts had more pronounced pulsatility compared to the entire carotid sinus, shown in Fig 36.

In the physiologic carotid model, changing the angle of stent orientation was found to influence wall stress values by 0.2%. However, for this carotid model, the deployed stent was completely encapsulated by the arterial wall and no degree of stent axial rotation influenced arterial wall stresses. Thus for the carotid models and stent designs considered, angle of stent orientation may not contribute to wall stress significantly as compared to other consequential parameters such as stent design and material models.

5.2.2.2.1.1 Stent diameter and its relation to wall stress

To evaluate the effect of stent expansion on arterial wall stresses, simulations were conducted with stent expanded to a range of diameters lesser and more than systolic sinus inner diameter (4.8 mm). This study was undertaken only with low flow rates boundary condition applied because these flow rates corresponded with the specific small dimensions of the carotid.

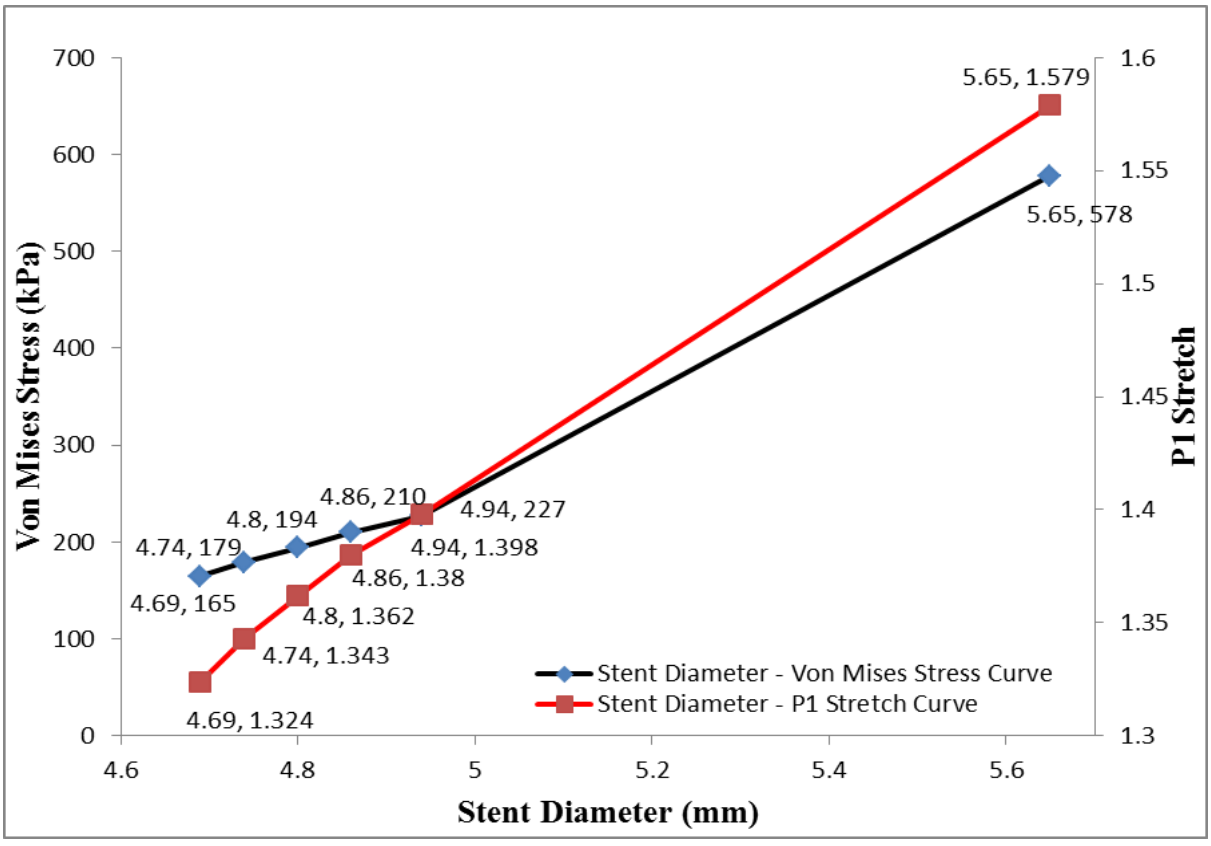

Chart 4. Variation of wall stress and principal circumferential stretch with stent diameter for carotid model CA3

Results indicated that for this diminutive carotid model, as stent diameter increased, wall stresses and wall stretch values increased linearly for the range of stent diameters 4.69-4.94 mm. For a stent diameter that was 20% more than systolic sinus inner diameter (for this case study, it was 4.94 mm), wall stretch was observed to increase by 6% and wall stress by 50%, compared to control, as mentioned earlier. There was approximately 37% difference in wall stress values between stent diameters of 4.69 mm and 4.94 mm, and 5% difference in wall stretch values for the same stent diameter range. Thus, for the considered diminutive carotid model and stent design, stent manufactured to expand to 4.69 mm would activate baroreceptors with the least amount of induced wall stress. However, since a stent manufactured to expand to 20% more than sinus systolic inner diameter anchors itself with the arterial wall, all results were procured and analyzed for the case of stent diameter 4.94 mm. In Chart 4, one more case study for stent diameter 5.65 mm (corresponding to approximately 40% more than systolic diameter) was conducted only to observe the trend in stent diameter and stress/stretch behavior when stent is over expanded.

5.2.2.2.1.2 Analysis of hemodynamic parameters – comparison between low flow rates and physiologic flow rates cases

For the stent deployed carotid model case with low flow rates, peak velocity of approximately 56 cm/s and 130 cm/s was observed along the ICA and ECA branches respectively, while velocity at the entrance of ECA, and at the heel of bifurcation, was 74 cm/s. For this unique carotid bifurcation geometry, stent deployment locally induced squeezing on the ECA entrance area, decreasing it by 28% and thereby increasing velocity of fluid entering ECA to 74 cm/s as opposed to 54 cm/s observed at the same region for the control case (diminutive carotid without stent). Such a comparison is better elicited in Fig 38. In case of the carotid with physiologic flow rates applied, ECA entrance velocity was elevated to 165 cm/s. Thus, stent deployment in this carotid model accelerated fluid at the heel of bifurcation, coinciding with ECA entrance.

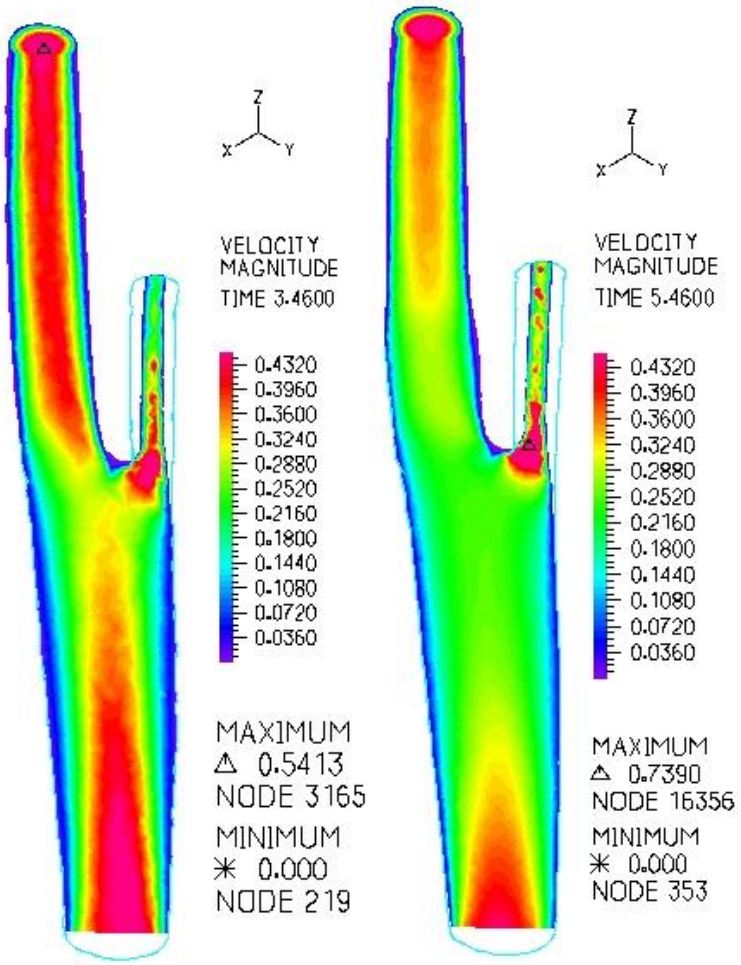

Figure 38. Velocity contour plots, shown at systole, for the carotid model with low flow rates. Shown on left is plot for control case study, while on the right is the carotid with stent deployed case. Plane for velocity contour representation is chosen for better visualization of peak velocity at ECA entrance alone and does not reflect the centerline peak velocity in the branches. Stent deployment induced an elevation of velocity at the entrance to ECA (peak of 74 cm/s) as compared to approximately 54 cm/s at the ECA entrance region of the control.

For stent deployed carotid with low flow rates, at the clinically significant region of carotid sinus, physiologic WSS value of approximately 16 dyn/cm^2 was observed. Stent deployment induced 16% reduction in WSS at the sinus corresponding to a decrease from approximately 19 dyn/cm^2 in the control to 16 dyn/cm^2. This was due to sinus cross-sectional area increase with stent deployment. No recirculation zones were observed for the small carotid

model irrespective of stent deployment. WSS in the CCA of stent deployed small carotid was in the range of 10-12 dyn/cm^2, compared to 1-2 dyn/cm^2 of the physiologic model. As flow rates were increased to physiologic levels for the small model, an elevation of WSS was observed. Simulations indicated WSS to be approximately 25-30 dyn/cm^2 in CCA and 32 dyn/cm^2 in the stent deployed sinus region.

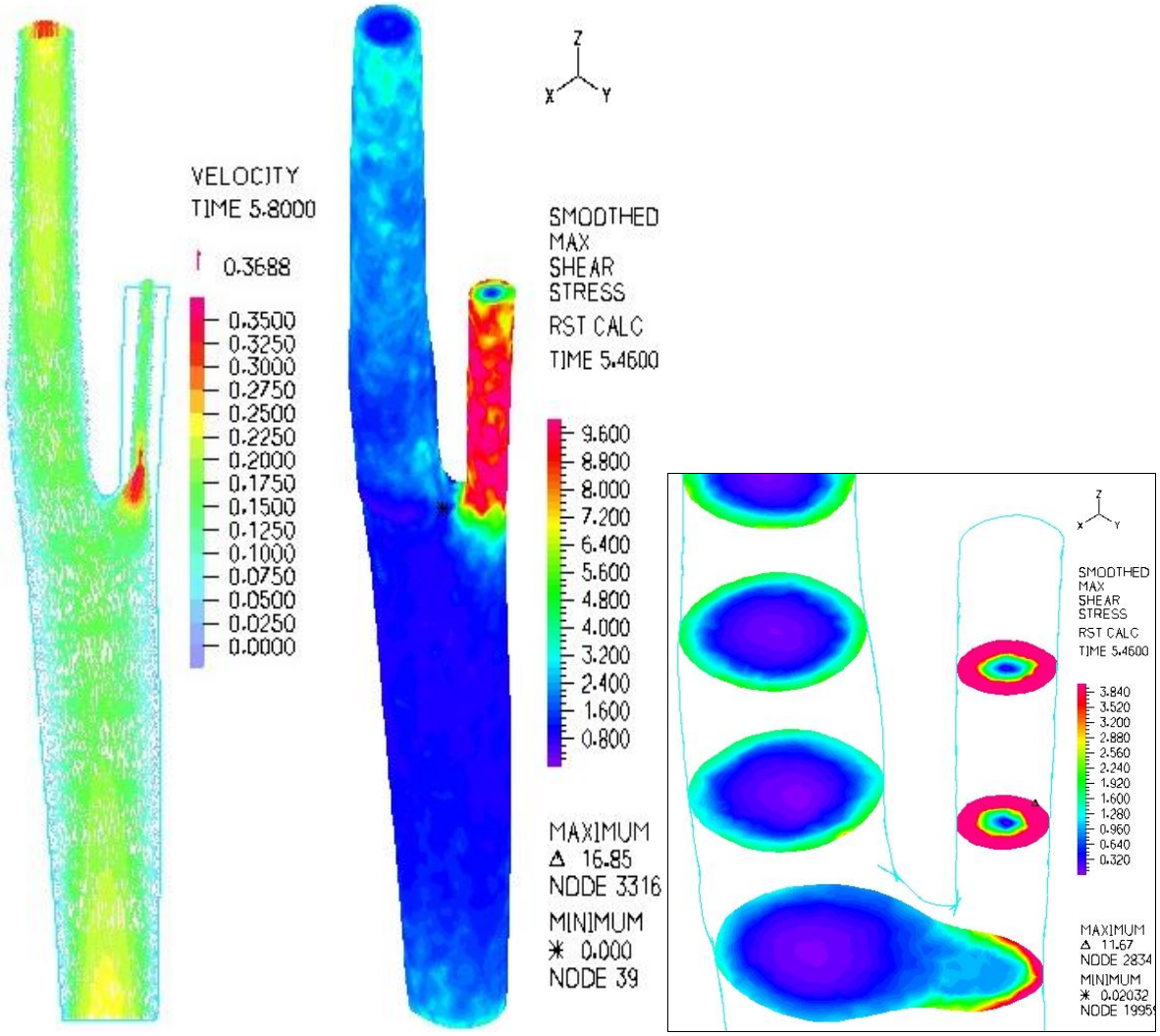

Figure 39. Velocity vector plot (left) shown for early diastole and wall shear stress contour (right) shown for peak systole of second carotid model. Inset shows WSS in the sinus region. Velocity decreased towards inner wall of CCA with no apparent recirculation zones visible. WSS in the sinus was observed to be approximately 16 dyn/cm^2 while it is 10-12 dyn/cm^2 in the CCA and 100 dyn/cm^2 in ECA.

5.2.2.3 Case Study 3 - Hypertensive condition simulation involving stent design D5 deployed in physiologic carotid model CA2

This case study was conducted as per requirements of specific aim #3. Model setup of case study 1 was used for this study. Fluid pressure boundary condition was increased to 147/113 mm Hg to simulate hypertensive conditions. Outlet velocity boundary conditions were not altered. Control case of carotid artery without device was simulated with the aforementioned hypertensive conditions. Post-simulation, systolic inner diameter of sinus was calculated. For the carotid case with device, stent was prescribed radial displacement boundary condition such that the expanded diameter of the stent would be 20% more than that of systolic inner diameter of control sinus. By this method, consistency in ratio of stent diameter to sinus diameter in both case studies 1 and 3 were maintained.

5.2.2.3.1 Results

To compare the effects of stent deployment on a carotid under hypertensive conditions, analysis of sinus wall stress, with and without device, were conducted. The comparative analysis is presented in Fig 40.

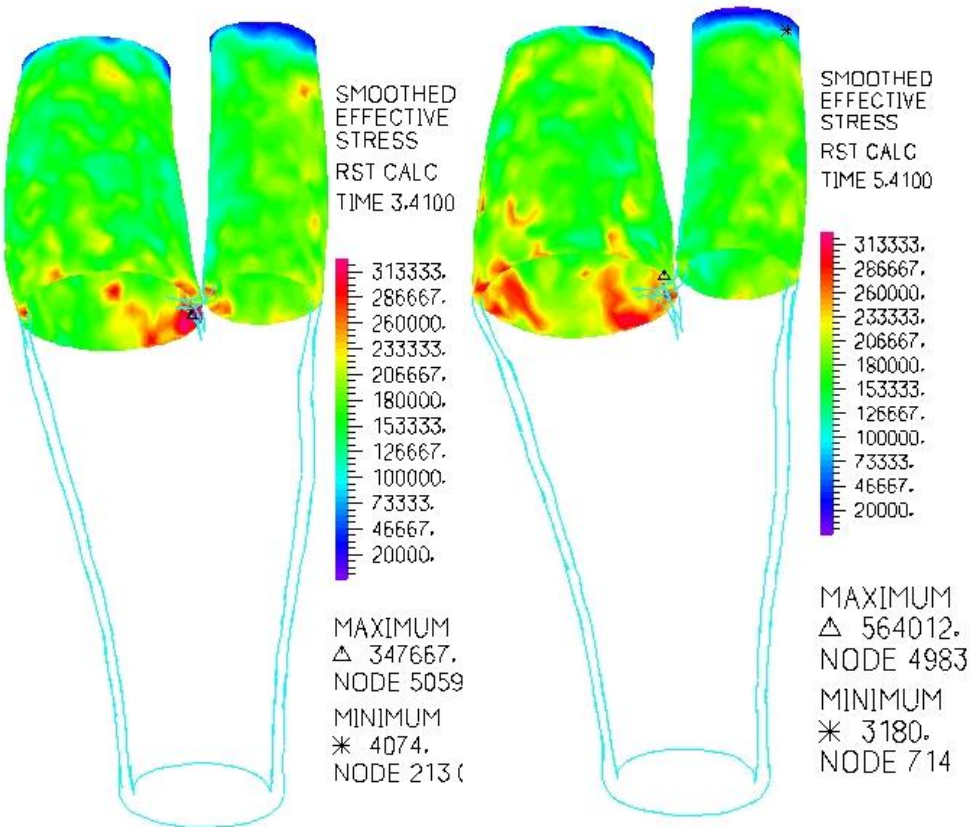

Figure 40. Comparison of wall stress in the sinus of carotid without stent (left) and with stent deployed (right). Peak wall stress due to stent deployment at the sinus was observed to be 564 kPa, while inherent stress in sinus of hypertensive carotid without any implants was approximately 348 kPa.

Inherent wall stress in the sinus of carotid, under hypertensive conditions and without any device deployed, is 348 kPa. Stent deployment increased sinus wall stress to 564 kPa, which is a 62% increase in localized wall stress compared to control. Corresponding to localized increase in wall stress, stent was also observed to induce an increase of 4% longitudinal stretch and 2.7% von Mises equivalent stretch. As the arterial wall was already under extensive circumferential stretching due to hypertensive flow, simulations predicted that stent deployment induced an additional circumferential wall stretch only at regions of wall directly in contact with stent struts. Such an additive stretching of sinus wall at regions of contact, decreased circumferential stretching of sections of sinus wall between the struts. When the entire sinus section was analyzed, it was observed that stent deployment had induced a 0.7% decrease in circumferential wall stretch compared to control. Consistent with the observation of case study 1, stent deployment did not adversely affect bifurcation wall stress in the hypertensive carotid. Bifurcation wall stress changed by only 0.07% for stent deployed carotid case compared to the hypertensive control. Furthermore, arterial wall compliance decreased by 65% due to stent deployment. Since compliance decreased significantly in this hypertensive case (65%) compared to normotensive case (22%), wall stretch pulsatility was evaluated to check if the device would have a long lasting effect on mitigation of hypertension.

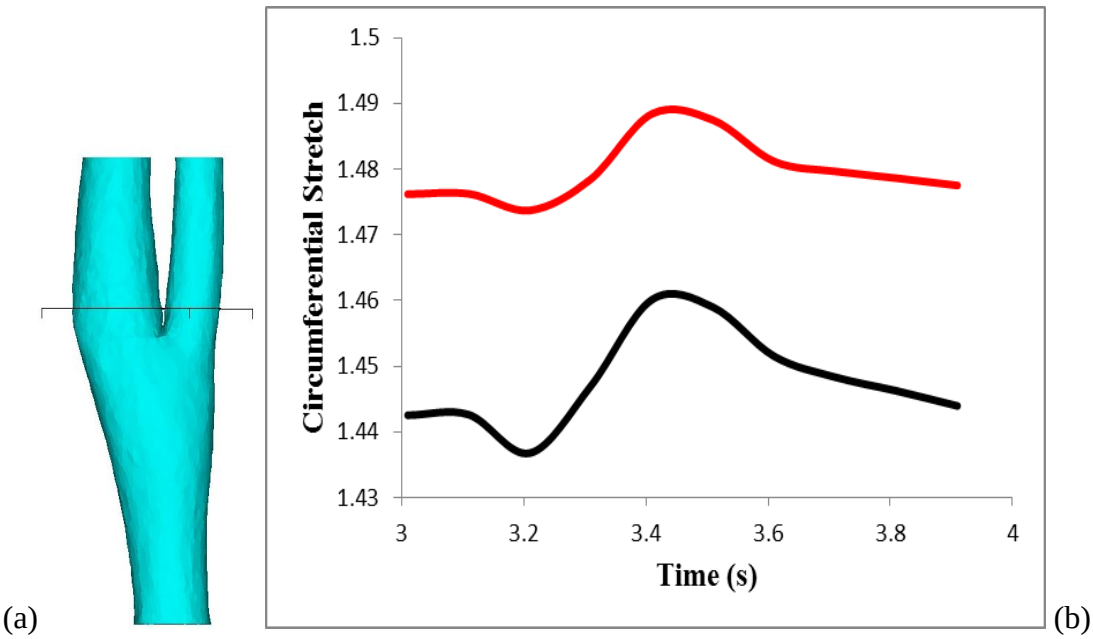

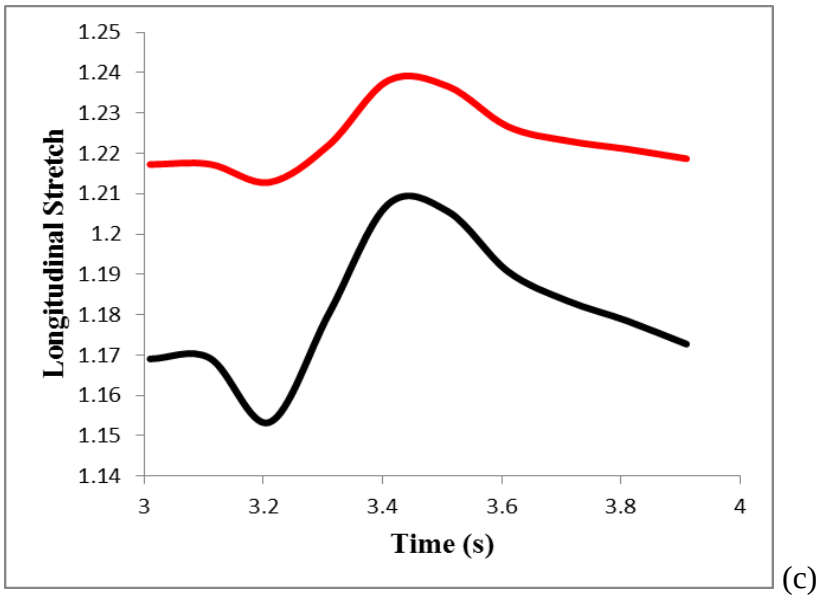

Figure 41. Section of carotid sinus, at the plane shown in (a), is chosen for analysis of time variance of wall stretch. Circumferential and longitudinal wall stretch variance with time are presented in (b) and (c). Wall stretch for control case is indicated in black while that for carotid with device is in red. Both control and device deployed cases had wall stretch pulsatility in synchroneity with pulsatility of blood flow.

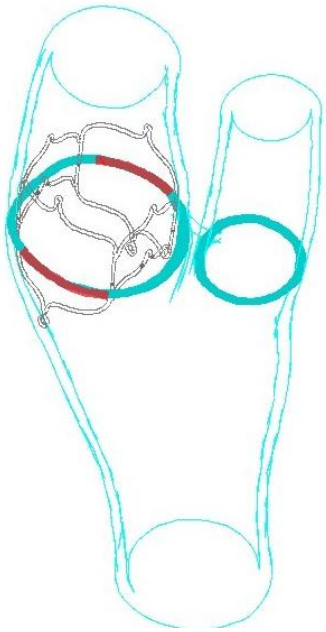

(a)

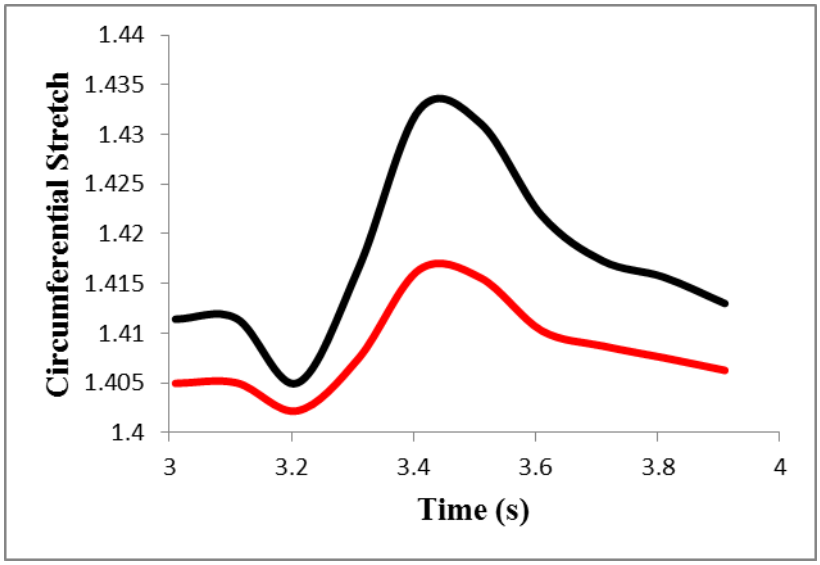

(b)

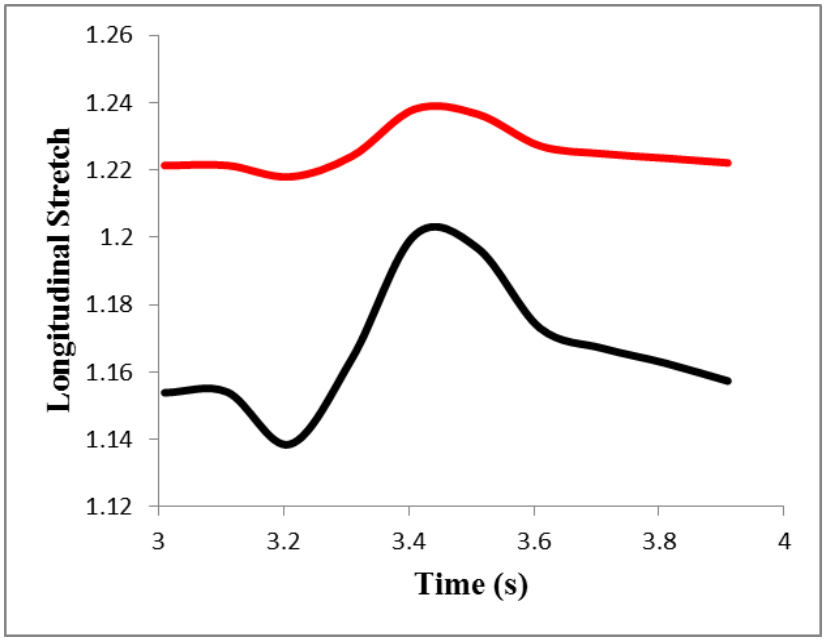

(c)

Figure 42. Section of sinus wall between stent struts, shown in (a) and indicated in red, is chosen for time variance wall stretch plots. Circumferential and longitudinal wall stretch variance with time are presented in (b) and (c). Wall stretch for control case is indicated in black while that for carotid with device is in red. Circumferential wall stretch for the device case was lower in magnitude compared to control. However, the device deployed carotid sinus wall exhibited both circumferential and longitudinal wall stretch pulsatility.

Accordingly, a plot of time variance of sinus wall stretch revealed that sinus of carotid with stent deployed had pulsatility in sync with cardiac cycle, as shown in Figs 41 and 42. Even with decreased compliance, stent deployed carotid sinus exhibited wall stretch pulsatility as shown in Fig 41. However, when the section of sinus wall between stent struts was analyzed, due to hypertensive flow conditions, the additive wall stretch due to device was at the points of contact with stent and not between stent struts, as explained earlier. This resulted in circumferential stretch of device deployed carotid to fall below that of control, as shown in Fig 42 a.. However, irrespective of plane of analysis, sinus of device deployed case exhibited wall stretch pulsatility.

5.2.2.3.1.1 Analysis of hemodynamic parameters

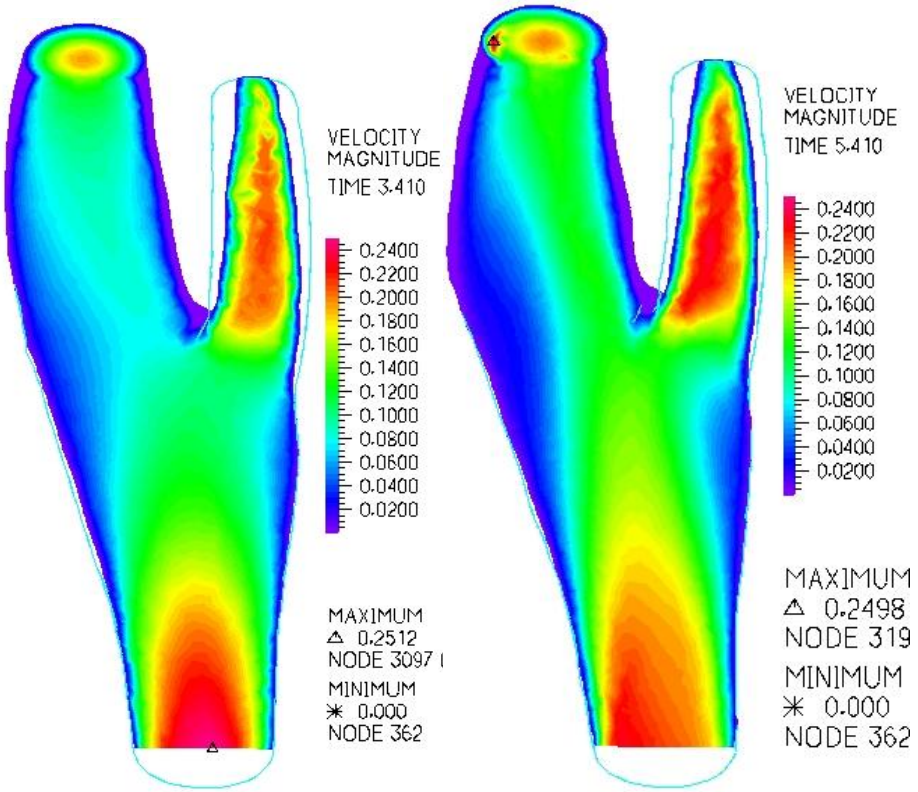

Figure 43. Velocity contour plots, shown at systole, for carotid without stent (left) and for stent deployed case (right). Systolic peak velocities in ICA and ECA, in both control and stent case, were 22 cm/s and 52 cm/s respectively. Stent deployment increased sinus area thereby enhancing flow separation at the sinus.

Since outlet velocity boundary conditions were not altered, no changes in velocity magnitudes were observed between control and stent deployed cases in both hypertensive and normotensive simulations. However, in hypertensive simulation, stent deployment induced flow separation at sinus region and common carotid branch as shown in Fig 43. This stent induced flow separation is more pronounced in hypertensive condition.

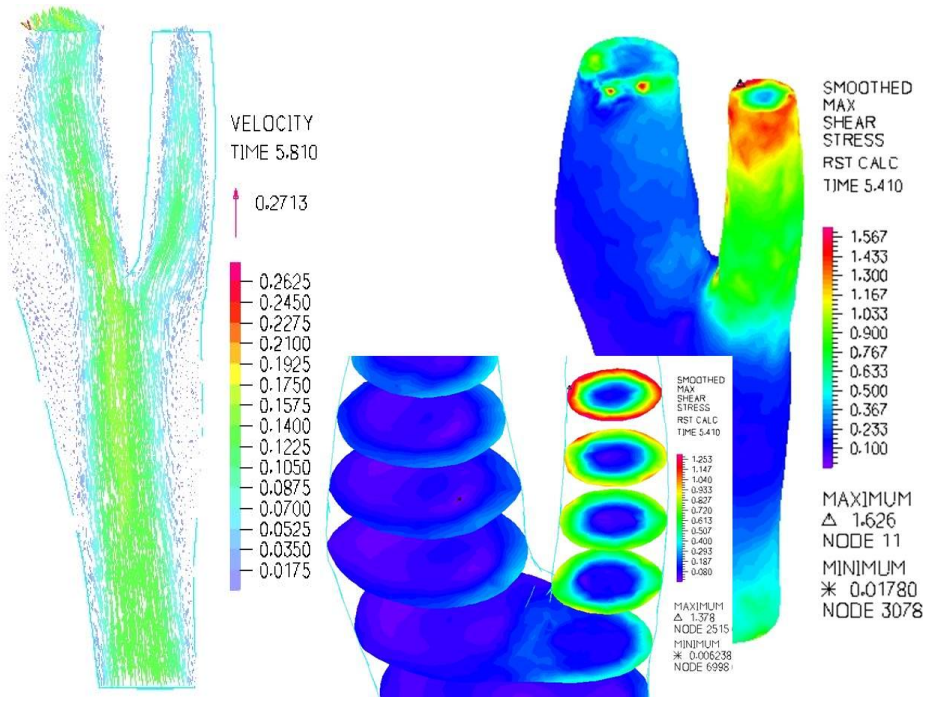

Figure 44. Velocity vector plot (left) shown for early diastole and wall shear stress contour (right) shown for peak systole. Inset shows WSS in the sinus region. Velocity vector analysis showed prominent recirculation zones in the sinus and CCA. WSS in the sinus was observed to be in the range of 3-4 dyn/cm^2 while it was 2-5 dyn/cm^2 in ICA and CCA, 10-13 dyn/cm^2 in ECA and 1-2 dyn/cm^2 at the recirculation zones.

Velocity vector analysis clearly revealed prominent recirculation zones in the carotid sinus and common carotid branch, as shown in Fig 44. Since velocity boundary conditions from normotensive were retained for this case study, simulations did not indicate significant WSS value changes, compared to normotensive study. A comparative analysis between control and device deployed case of carotid sinus showed that stent deployment did not adversely affect sinus WSS and values were in the range of 3-4 dyn/cm^2 in both cases.

VI. Discussion of extravascular and endovascular device case studies

Consequential results of the simulations are that both extravascular and endovascular stent-type devices induce localized stretching of sinus, thereby elevating wall stresses in those regions. This conforms to the trend observed in preliminary case studies. Using FSI simulations, the extent of wall stretch as well as associated stress development have been quantified on case by case basis. It was observed that as wall stress increased from 198 kPa to 242 kPa due to extravascular device clamping on the physiologic carotid model, circumferential wall stretch decreased by 7%. Longitudinal wall stretch increased thereby elevating von Mises equivalent stretch by 3%. However, stent deployment on the same model elevated inherent sinus stress values from 198 kPa to 237 kPa, corresponding to 2.5% increase in circumferential wall stretch, 7.5% increase in longitudinal stretch and therefore a 6% increase in von Mises equivalent stretch. Thus, endovascular stents induced better elevation of wall stretch compared to extravascular devices. Endovascular stents consistently induced localized increase in sinus wall stretch even in extreme carotid models, as shown by simulation results of the diminutive carotid. Stent induced 6% increase in circumferential and longitudinal stretch, corresponding to a 54% increase in sinus wall stress, all in comparison to control. Even under hypertensive conditions, the stent induced localized increase in sinus wall stretch thereby indicating the efficacy of such endovascular stent designs under a range of conditions. Further discussion in this section pertains to the detailed analysis of efficacy of both extravascular and endovascular device types, from all perspectives of structural biomechanics and hemodynamics.

Since baroreceptors respond to induced wall stretch, devices are deployed at the sinus and wall biomechanics parameters are evaluated that region. However, to investigate any adverse effects due to device deployment on the carotid, wall stresses were analyzed for the overall carotid models as well. Invariably in all cases, peak stresses occurred at the bifurcation region, close to ECA entrance. Location of peak stress did not vary and was not influenced by the presence or absence of device at the sinus. Variations in peak stress values were however observed depending on device deployment. For the physiologic carotid case with extravascular device, bifurcation peak stress increased by 7% due to device deployment at sinus. Such an elevation of bifurcation peak stress is attributed to the compressive effect of device at the sinus and the rubber-like material properties of the arterial wall. Bifurcation region being the stagnation point for fluid flow contributes to stress development close to the bifurcation.

Clamping of sinus region by the extravascular device reduces sinus flow area which in turn enhances fluid stagnation at the bifurcation region, thereby elevating wall stresses there. For the physiologic carotid model with stent deployed case, bifurcation peak stress was not significantly altered by deployment. Stent was observed to induce only a 0.6% increase in bifurcation stress, while for the diminutive carotid model, bifurcation stress was observed to increase from 211 kPa to 622 kPa. Such an exacerbation of stress for the diminutive carotid is hypothesized to be the combined effect of flow conditions and unique carotid geometry. The unique diminutive carotid model represents extreme worst case scenario from geometry perspective, as the model is streamlined, devoid of characteristic sinus bulge, and the ICA and ECA branches are in close proximity to each other post-bifurcation. As mentioned earlier, such a unique carotid was primarily considered to evaluate device efficacy for extreme model conditions that may be present in certain individuals. However, with such models, there is a possibility that device deployment might induce adverse structural or hemodynamic parameter changes that might not otherwise be induced in physiologic carotids. Accordingly, in the diminutive model, due to the close proximity of ICA and ECA branches, device deployment in ICA increases sinus area by 16%, thereby reducing ECA entrance area by 28% and accelerating fluid at its entrance. Such area restriction in ECA branch, coupled with high velocity at its entrance, compounds bifurcation stress resulting in increase in bifurcation stress from 211 kPa to 622 kPa. It is reiterated that such exacerbation of stress is due to the unique streamlined geometry and that such adverse effects do not reflect conditions in physiologic carotids with characteristic contours.

As peak stress values at bifurcation do not influence hypertension treatment therapy, they were analyzed only to check for adverse effects due to device deployment. Thus, for the carotid models and devices evaluated, endovascular stent type devices deployed in physiologic carotid models performed better by inducing localized elevation of sinus wall stress without adversely affecting wall biomechanics elsewhere. This claim holds good even in hypertensive cases.

It had been mentioned earlier that baroreceptors respond to elevated wall stress values and adapt to such elevated states if the induced stimulus is static. All simulations conducted were scrutinized to check if device deployment induced a static or pulsatile wall stretch stimuli on the sinus region. Such an evaluation would shed light on the efficacy of device over a long period of time. Post-simulation analysis revealed a significant pulsatility of wall stretch for the stent type

device deployed in both the physiologic and diminutive carotid models. Such a pulsating effect was conspicuously absent for the extravascular device case wherein the struts of the device were observed to severely clamp the sinus section leaving no room for wall to pulsate. Such clamping of sinus was compensated by the arterial wall undergoing significant expansion upstream of device, at the CCA region. Deploying an extravascular device therefore might initially activate baroreceptors to respond to the applied wall stretch. However, for long term benefits of device based therapy for hypertension, stent type devices are predicted to be better as justified by the pulsating effect of device induced wall stretch. Further strengthening the contention in favor of stent type devices are their efficacy in inducing localized increase in wall stretch and stress without adversely affecting flow domain hemodynamics. Simulation results clearly indicate that these devices, when deployed in physiologic carotids, have only a marginal influence on velocity profile and WSS. They have been consistent in not inducing adverse effects in both physiological and pathological conditions. Though, these devices induce a decrease in sinus WSS for the extreme diminutive model, such an adverse effect is attributed to the unique carotid model and not the device type. Thus, stent type devices perform better in inducing mechanical stretch stimuli without adversely affecting hemodynamics, suggesting that they may be efficient biomedical devices in reducing hypertension.

Having evaluated the efficacy of each device, it is imperative to validate the simulation results obtained. It is not pragmatic to replicate device deployment in carotid artery *in vitro* and subsequently conduct structural and hemodynamic analysis on such a model. However, verification of our control case simulation results with prior studies would serve as a means of validating our methodology and thereby the predictions made regarding response of carotid artery to device deployment. Control case results of the physiologic carotid model are observed to be consistent with previously reported solids-only static pressurization simulation and other FSI simulations. Delfino et al report stress on the inner walls of carotid sinus to be 220 kPa [74] which is in the range of simulation generated results (198 kPa in sinus of control case). Leach et al report principal wall stress on pre-rupture ECA branch to be 202 kPa [75] while our simulations predict stress in the same branch to be approximately 229 kPa. Consistency of fluid domain results with literature data is also observed. Low WSS is reported to be prevalent in carotid sinus of physiologic models [76-78] and recirculation zones, coinciding with such low WSS regions, have been observed in similar numerical simulation studies [79]. Flow patterns,

especially formation of recirculation zones, conform with early prominent studies by Karino, Goldsmith et al [80]. Thus, consistency of results with previously published data serve as an indirect means of validation of our simulations.

VII. Limitations

1) Principal objective of stretching carotid sinus using devices is to mechanically induce baroreceptor activation. However, in this study, we do not test the translation of carotid sinus stretching to baroreceptor stimulation and thereby baroreflex activation. Though this is an inherent limitation of the study, predicting response of baroreceptors or components of baroreflex is beyond the scope of this study. If such a numerical study is conducted, it would entail multi-scale modeling of all tissues, organs as well as the biochemical pathway of baroreflex. However, such an advanced study may provide a lot of information that may not essentially address the question of device efficacy in a vascular environment, from a simulation perspective. For a complete analysis of efficacy of device deployment, these devices could be subjected to clinical trials following our numerical evaluation.

2) Evaluation of the effects of extravascular and endovascular device deployment on carotid artery was conducted on subject derived carotid models and not patient specific models. The carotid models were devoid of inherent physiologic vascular components such as lipid pool, calcifications etc. Such simplifications of carotid model for evaluating effects of device deployment make this study a 'subject derived parametric study' rather than a patient specific one. Objective of future work would be to evaluate effects of device deployment on patient specific carotid models, with all vascular components incorporated.

3) One other important component that makes this a subject derived study is the lack of variable wall thickness that is inherent in physiologic carotid arteries. The physiologic carotid model simulated in this study had a uniform wall thickness of approximately 0.8mm. Furthermore, the components of vessel wall, such as intima, media and adventitia were not modeled separately. To reduce complications, carotid wall was modeled as a single layer of isotropic Mooney-Rivlin material.

4) It has been shown earlier by our lab group that isotropic formulation under predicts wall stress values compared to anisotropic formulation [81]. However, the trend of elevated wall stress values due to device deployment would be persistent with both formulations. Thus, for this parametric study, arterial wall was modeled as isotropic material.

5) Fluid domain had been modeled to be laminar. Although the Reynolds number of flow inside physiologic carotid arteries categorizes the flow to be laminar, due to cardiac pulsatility and contours of the carotid artery, blood flow experiences turbulence. Modeling flow domain as turbulent may be a better representation as it may predict accentuated recirculation zones, but it may not necessarily have consequential effects on arterial wall stress. Since objective of the study was to evaluate wall stretch/stress due to device deployment, modeling fluid as turbulent did not warrant justification. However, modeling flow as laminar is acknowledged as a limitation of the study.

6) Lack of model specific boundary conditions, for both normotensive and hypertensive simulations, had to be compensated by referencing previously published boundary condition values. Though these referenced values were experimentally measured in healthy subjects, they do not pertain to the specific carotid models considered, making the lack of pertinent boundary conditions a significant limitation of the study.

7) In this study, modeling stents as a linear elastic material (stainless steel) is a generalization of the principle of operation, whereas stents are in fact nitinol based. This study lays ground work for more rigorous future studies in which the complex material behavior of nitinol would be incorporated. Though modeling the device as nitinol might lower device induced biomechanical values, the observed trend of elevation of wall stretch and stress due to device deployment would prevail.

8) Lack of validation of simulation results is an important limitation of the study. Though our structural analyses and hemodynamic results correlate well with previously published literature data, lack of a comprehensive validation study is acknowledged as a limitation. This limitation too would be addressed in future work.

VIII. Conclusion

In this study, extents of arterial wall stretch and corresponding stress development due to different device type deployment have been numerically quantified. Effects of deployment on associated flow domain hemodynamics have also been analyzed which, when combined with structural biomechanical parameters of stretch and stress, serve as yardsticks for device performance evaluation. Based on simulation results and criteria for evaluation, stent type devices are predicted to be more efficient and have a long term effect in mitigating hypertension compared to extravascular device types. Furthermore, these stents are also predicted to perform their function efficiently without inducing adverse effects, even under pathological hypertensive conditions.

From a broader perspective, the presented results demonstrate the ability of our FSI - coupled with contact surface methodology - to predict response of carotid arteries to device deployment, and indirectly evaluate the therapeutic viability of such devices in hypertension treatment.

Further studies with varying stent designs and different patient specific geometries would contribute to the development of this numerical methodology as a sturdy procedure in evaluation and optimization of endovascular mechanical device designs for hypertension treatment therapies on case by case basis.

References

1. **K. Wolf-Maier, R.S. Cooper, J.R. Banegas, S. Giampaoli, H.W. Hense, M. Joffres, M. Kastarinen, N. Poulter, P. Primatesta, F. Rodriguez-Artalejo, B. Stegmayr, M. Thamm, J. Tuomilehto, D. Vanuzzo, and F. Vescio, *Hypertension, prevalence and blood pressure levels in 6 European countries, Canada, and the United States.* Jama-Journal of the American Medical Association, 2003. 289(18): p. 2363-2369.**

2. **V. Perkovic, R. Huxley, Y.F. Wu, D. Prabhakaran, and S. MacMahon, *The burden of blood pressure-related disease - A neglected priority for global health.* Hypertension, 2007. 50(6): p. 991-997.**

3. **S. Balu, *Incremental cost of treating hypertension in the United States*. 2005, Purdue University. p. 140.**

4. **D.A. Calhoun, D. Jones, S. Textor, D.C. Goff, T.P. Murphy, R.D. Toto, A. White, W.C. Cushman, W. White, D. Sica, K. Ferdinand, T.D. Giles, B. Falkner, and R.M. Carey, *Resistant hypertension: Diagnosis, evaluation, and treatment - A Scientific Statement from the American Heart Association Professional Education Committee of the Council for High Blood Pressure Research.* Hypertension, 2008. 51(6): p. 1403-1419.**

5. **J.F. Setaro and H.R. Black, *Current Concepts - Refractory Hypertension.* New England Journal of Medicine, 1992. 327(8): p. 543-547.**

6. **M. Schuenke, E. Schulte, U. Schumacher, L. Ross, and E. Lamperti, *Atlas of anatomy: neck and internal organs*. 2006: Thieme.**

7. **C.H. Davos, L.C. Davies, and M. Piepoli, *The Effect of Baroreceptor Activity on Cardiovascular Regulation.* The Hellenic Journal of Cardiology, 2002. 43: p. 145-155.**

8. **M.P. Jaypee Brothers, *Textbook of Anatomy with Colour Atlas by Inderbir Singh*. 2007: Jaypee Brothers, Medical Publishers.**

9. **P.M. Rees, *Observations on Fine Structure and Distribution of Presumptive Baroreceptor Nerves at Carotid Sinus.* Journal of Comparative Neurology, 1967. 131(4): p. 517-547.**

10. **A.J. JE, *The Effects of Changes of Extramural, Intrathoracic, Pressure on Aortic Arch Baroreceptors.* Journal of Physiology-London, 1971. 214(1): p. 89-103.**

11. **H.W. Ead, J.H. Green, and E. Neil, *A Comparison of the Effects of Pulsatile and Non-Pulsatile Blood Flow through the Carotid Sinus on the Reflexogenic Activity of the Sinus Baroceptors in the Cat.* Journal of Physiology-London, 1952. 118(4): p. 509-519.**

12. **P.M. Rees and P. Jepson, *Measurement of Arterial Geometry and Wall Composition in Carotid Sinus Baroreceptor Area.* Circulation Research, 1970. 26(4): p. 461-467.**

13. **R.J. Bagshaw and G.M. Fischer, *Morphology of Carotid Sinus in Dog.* Journal of Applied Physiology, 1971. 31(2): p. 198-202.**

14. **P.B. Dobrin, *Mechanical-Properties of Arteries.* Physiological Reviews, 1978. 58(2): p. 397-460.**

15. **R. Klabunde, *Cardiovascular physiology concepts*. 2005: Lippincott Williams & Wilkins.**

16. **K. Chung and H. Chung, *Gross anatomy*. 2007: Lippincott Williams & Wilkins.**

17. **G. Hajduczok, M.W. Chapleau, R.J. Ferlic, H.Z. Mao, and F.M. Abboud, *Gadolinium Inhibits Mechanoelectrical Transduction in Rabbit Carotid Baroreceptors - Implication of Stretch-Activated Channels.* Journal of Clinical Investigation, 1994. 94(6): p. 2392-2396.**

18. **J.T. Cunningham, R.E. Wachtel, and F.M. Abboud, *Mechanosensitive Currents in Putative Aortic Baroreceptor Neurons in-Vitro.* Journal of Neurophysiology, 1995. 73(5): p. 2094-2098.**

19. **J.T. Cunningham, R.E. Wachtel, and F.M. Abboud, *Mechanical stimulation of neurites generates an inward current in putative aortic baroreceptor neurons in vitro.* Brain Research, 1997. 757(1): p. 149-154.**

20. **N. Tavernarakis and M. Driscoll, *Molecular modeling of mechanotransduction in the nematode Caenorhabditis elegans.* Annual Review of Physiology, 1997. 59: p. 659-689.**

21. **H.A. Drummond, M.P. Price, M.J. Welsh, and F.M. Abboud, *A molecular component of the arterial baroreceptor mechanotransducer.* Neuron, 1998. 21(6): p. 1435-1441.**

22. **V. Snitsarev, C.A. Whiteis, M.W. Chapleau, and F.M. Abboud, *Mechano- and chemosensitivity of rat nodose neurones - selective excitatory effects of prostacyclin.* Journal of Physiology-London, 2007. 582(1): p. 177-194.**

23. **M.W. Chapleau, J.T. Cunningham, M.J. Sullivan, R.E. Wachtel, and F.M. Abboud, *Structural Versus Functional Modulation of the Arterial Baroreflex.* Hypertension, 1995. 26(2): p. 341-347.**

24. **F.M. Abboud, *The Sympathetic System in Hypertension - State-of-the-Art Review.* Hypertension, 1982. 4(3): p. 208-225.**

25. **A.M. Brown, *Receptors under Pressure - Update on Baroreceptors.* Circulation Research, 1980. 46(1): p. 1-10.**

26. **J. Zhang and S.W. Mifflin, *Differential roles for NMDA and non-NMDA receptor subtypes in baroreceptor afferent integration in the nucleus of the solitary tract of the rat.* Journal of Physiology-London, 1998. 511(3): p. 733-745.**

27. **J.L. Seagard, C. Dean, and F.A. Hopp, *Neurochemical transmission of baroreceptor input in the nucleus tractus solitarius.* Brain Research Bulletin, 2000. 51(2): p. 111-118.**

28. **J. Pamidimukkala and M. Hay, *Frequency dependence of endocytosis in aortic baroreceptor neurons and role of group III mGluRs.* American Journal of Physiology-Heart and Circulatory Physiology, 2001. 281(1): p. H387-H395.**

29. **Z. Liu, C.Y. Chen, and A.C. Bonham, *Metabotropic glutamate receptors depress vagal and aortic baroreceptor signal transmission in the NTS.* American Journal of Physiology-Heart and Circulatory Physiology, 1998. 44(5): p. H1682-H1694.**

30. **C. Pawloskidahm and F.J. Gordon, *Evidence for a Kynurenate-Insensitive Glutamate Receptor in Nucleus-Tractus-Solitarii.* American Journal of Physiology, 1992. 262(5): p. H1611-H1615.**

31. **P.M. Pilowsky and A.K. Goodchild, *Baroreceptor reflex pathways and neurotransmitters: 10 years on.* Journal of Hypertension, 2002. 20(9): p. 1675–1688.**

32. **R.A.L. Dampney, *Functional-Organization of Central Pathways Regulating the Cardiovascular-System.* Physiological Reviews, 1994. 74(2): p. 323-364.**

33. **J. Chalmers, L. Arnolda, I. Llewellynsmith, J. Minson, P. Pilowsky, and S. Suzuki, *Central Neurons and Neurotransmitters in the Control of Blood-Pressure.* Clinical and Experimental Pharmacology and Physiology, 1994. 21(10): p. 819-829.**

34. **Y.W. Li, Z.J. Gieroba, R.M. Mcallen, and W.W. Blessing, *Neurons in Rabbit Caudal Ventrolateral Medulla Inhibit Bulbospinal Barosensitive Neurons in Rostral Medulla.* American Journal of Physiology, 1991. 261(1): p. R44-R51.**

35. **S.L. Cravo and S.F. Morrison, *The Caudal Ventrolateral Medulla Is a Source of Tonic Sympathoinhibition.* Brain Research, 1993. 621(1): p. 133-136.**

36. **G. Drolet, J. Chalmers, and W. Blessing, *Vasodepressor Neurons in Medulla Alter Cardiac Contractility and Cardiac-Output.* Hypertension, 1993. 21(2): p. 210-215.**

37. **R.A.L. Dampney, W.W. Blessing, and E. Tan, *Origin of Tonic Gabaergic Inputs to Vasopressor Neurons in the Subretrofacial Nucleus of the Rabbit.* Journal of the Autonomic Nervous System, 1988. 24(3): p. 227-239.**

38. **W.W. Blessing, *Depressor Neurons in Rabbit Caudal Medulla Act Via Gaba Receptors in Rostral Medulla.* American Journal of Physiology, 1988. 254(4): p. H686-H692.**

39. **C.A. Ross, D.M. Armstrong, D.A. Ruggiero, V.M. Pickel, T.H. Joh, and D.J. Reis, *Adrenaline Neurons in the Rostral Ventrolateral Medulla Innervate Thoracic Spinal-Cord - a Combined Immuno-Cytochemical and Retrograde Transport Demonstration.* Neuroscience Letters, 1981. 25(3): p. 257-262.**

40. **B.J. Oldfield and E.M. Mclachlan, *An Analysis of the Sympathetic Preganglionic Neurons Projecting from the Upper Thoracic Spinal Roots of the Cat.* Journal of Comparative Neurology, 1981. 196(2): p. 329-345.**

41. **J. Ciriello and F.R. Calaresu, *Distribution of Vagal Cardioinhibitory Neurons in the Medulla of the Cat.* American Journal of Physiology, 1980. 238(1): p. R57-R64.**

42. **V.L. Cooper and R. Hainsworth, *Carotid baroreceptor reflexes in humans during orthostatic stress.* Experimental Physiology, 2001. 86(5): p. 677-681.**

43. **M.T. La Rovere, G.D. Pinna, and G. Raczak, *Baroreflex sensitivity: Measurement and clinical implications.* Annals of Noninvasive Electrocardiology, 2008. 13(2): p. 191-207.**

44. **S.C. Walgenbach and J.T. Shepherd, *Role of Arterial and Cardiopulmonary Mechanoreceptors in the Regulation of Arterial-Pressure during Rest and Exercise in Conscious Dogs.* Mayo Clinic Proceedings, 1984. 59(7): p. 467-475.**

45. **S.F. Vatner, D. Franklin, Vancitte.Rl, and Braunwal.E, *Effects of Carotid Sinus Nerve Stimulation on Coronary Circulation of Conscious Dog.* Circulation Research, 1970. 27(1): p. 11-21.**

46. **M.J. Joyner, *Baroreceptor function during exercise: resetting the record.* Experimental Physiology, 2006. 91(1): p. 27-36.**

47. S. Ogoh, W.L. Wasmund, D.M. Keller, O.Y. A, K.M. Gallagher, J.H. Mitchell, and P.B. Raven, *Role of central command in carotid baroreflex resetting in humans during static exercise.* J Physiol, 2002. 543(Pt 1): p. 349-64.

48. J.W. McCubbin, J.H. Green, and I.H. Page, *Baroreceptor function in chronic renal hypertension.* Circulation Research, 1956. 4: p. 205-210.

49. M.W. Chapleau, G. Hajduczok, and F.M. Abboud, *Mechanisms of Resetting of Arterial Baroreceptors - an Overview.* American Journal of the Medical Sciences, 1988. 295(4): p. 327-334.

50. S.D. Navaneethan, T.E. Lohmeier, and J.D. Bisognano, *Baroreflex stimulation: A novel treatment option for resistant hypertension.* Journal of the American Society of Hypertension, 2009. 3(1): p. 69-74.

51. D. Mendelowitz and A.M. Scher, *Pulsatile Sinus Pressure Changes Evoke Sustained Baroreflex Responses in Awake Dogs.* American Journal of Physiology, 1988. 255(3): p. H673-H678.

52. A.M. Bilgutay and C.W. Lillehei, *Treatment of Hypertension with an Implantable Electronic Device.* Journal of the American Medical Association, 1965. 191(8): p. 649-653.

53. S.I. Schwartz, L.S. Griffith, A. Neistadt, and N. Hagfors, *Chronic Carotid Sinus Nerve Stimulation in Treatment of Essential Hypertension.* American Journal of Surgery, 1967. 114(1): p. 5-15.

54. T.K. Peters, H.E. Koralewski, and E. Zerbst, *The Principle of Electrical Carotid-Sinus Nerve-Stimulation - a Nerve Pacemaker System for Angina-Pectoris and Hypertension Therapy.* Annals of Biomedical Engineering, 1980. 8(4-6): p. 445-458.

55. T.E. Lohmeier, E.D. Irwin, M.A. Rossing, D.J. Serdar, and R.S. Kieval, *Prolonged activation of the baroreflex produces sustained hypotension.* Hypertension, 2004. 43(2): p. 306-311.

56. **T.E. Lohmeier, T.M. Dwyer, D.A. Hildebrandt, E.D. Irwin, M.A. Rossing, D.J. Serdar, and R.S. Kieval, *Influence of prolonged baroreflex activation on arterial pressure in angiotensin hypertension.* Hypertension, 2005. 46(5): p. 1194-1200.**

57. **J. Bisognano, J. Sloand, V. Papademetriou, M. Rothstein, D. Sica, J. Flack, T.L. Pertile, R. Kieval, and R.J. Cody, *An implantable carotid sinus baroreflex activating system for drug-resistant hypertension: Interim chronic efficacy results from the multi-center rheos feasibility trial.* Circulation, 2006. 114(18): p. 575-575.**

58. **J.H.M. Tordoir, I. Scheffers, J. Schmidli, H. Savolainen, U. Liebeskind, B. Hansky, U. Herold, E. Irwin, A.A. Kroon, P. de Leeuw, T. Peters, R. Kieval, and R. Cody, *An Implantable Carotid Sinus Baroreflex Activating System: Surgical Technique and Short-Term Outcome from a Multi-Center Feasibility Trial for the Treatment of Resistant Hypertension.* European Journal of Vascular and Endovascular Surgery, 2007. 33: p. 414-421.**

59. **M.P. Schlaich, P.A. Sobotka, H. Krum, R. Whitbourn, A. Walton, and M.D. Esler, *Renal Denervation as a Therapeutic Approach for Hypertension Novel Implications for an Old Concept.* Hypertension, 2009. 54(6): p. 1195-1201.**

60. **H. Krum, M. Schlaich, R. Whitbourn, P.A. Sobotka, J. Sadowski, K. Bartus, B. Kapelak, A. Walton, H. Sievert, S. Thambar, W.T. Abraham, and M. Esler, *Catheter-based renal sympathetic denervation for resistant hypertension: a multicentre safety and proof-of-principle cohort study.* Lancet, 2009. 373(9671): p. 1275-1281.**

61. **J.B. Thomas, L. Antiga, S.L. Che, J.S. Milner, D.A. Steinman, J.D. Spence, and B.K. Rutt, *Variation in the carotid bifurcation geometry of young versus older adults: implications for geometric risk of atherosclerosis.* Stroke, 2005. 36(11): p. 2450-6.**

62. **D.L. Tang, C. Yang, S. Mondal, F. Liu, G. Canton, T.S. Hatsukami, and C. Yuan, *A negative correlation between human carotid atherosclerotic plaque progression and plaque wall stress: In vivo MRI-based 2D/3D FSI models.* Journal of Biomechanics, 2008. 41(4): p. 727-736.**

63. **Y. Alemu, *Numerical Modeling of Blood Flow in Prosthetic Heart Valves and Cardiovascular Pathologies*, in *Biomedical Engineering*. 2010, Stony Brook University: Stony Brook. p. 114.**

64. **L. Gardner, *The use of stainless steel in structures.* Progress in Structural Engineering and Materials, 2005. 7(2): p. 45-55.**

65. **K. Bathe, *Finite element procedures*. 1996: Prentice Hall.**

66. **K.J. Bathe and P.A. Bouzinov, *On the constraint function method for contact problems.* Computers & Structures, 1997. 64(5-6): p. 1069-1085.**

67. **H. Gao, Q. Long, M. Graves, J.H. Gillard, and Z.Y. Li, *Carotid arterial plaque stress analysis using fluid-structure interactive simulation based on in-vivo magnetic resonance images of four patients.* Journal of Biomechanics, 2009. 42(10): p. 1416-1423.**

68. **H. Zhang and K.J. Bathe, *Direct and iterative computing of fluid flows fully coupled with structures*, in *Computational Fluid and Solid Mechanics*, K.J. Bathe, Editor. 2001, Elsevier Science Ltd.: Cambridge, Mass.**

69. **ADINA, *ADINA Theory and Modeling Guide*. 2000: Watertown, MA.**

70. **F. Hansen, P. Mangell, B. Sonesson, and T. Lanne, *Diameter and compliance in the human common carotid artery--variations with age and sex.* Ultrasound in medicine & biology, 1995. 21(1): p. 1-9.**

71. **M. Trott, *The Mathematica guidebook for symbolics*. 2006: Springer.**

72. **H.R. Kirchheim, *Systemic arterial baroreceptor reflexes.* Physiological Reviews, 1976. 56(1): p. 100-176.**

73. **I. Thomas Edward Claiborne, *Development and evaluation of a catheter deliverable artificial aortic heart valve prosthesis and delivery system*, in *Biomedical Engineering*. 2008, Florida International University: Miami, Florida. p. 189.**

74. **A. Delfino, N. Stergiopulos, J.E. Moore, and J.J. Meister, *Residual strain effects on the stress field in a thick wall finite element model of the human carotid bifurcation.* Journal of Biomechanics, 1997. 30(8): p. 777-786.**

75. **J.R. Leach, V.L. Rayz, B. Soares, M. Wintermark, M.R.K. Mofrad, and D. Saloner, *Carotid Atheroma Rupture Observed In Vivo and FSI-Predicted Stress Distribution Based on Pre-rupture Imaging.* Annals of Biomedical Engineering, 2010. 38(8): p. 2748-2765.**

76. **J.S. Milner, J.A. Moore, B.K. Rutt, and D.A. Steinman, *Hemodynamics of human carotid artery bifurcations: Computational studies with models reconstructed from magnetic resonance imaging of normal subjects.* Journal of Vascular Surgery, 1998. 28(1): p. 143-156.**

77. **D.N. Ku, D.P. Giddens, C.K. Zarins, and S. Glagov, *Pulsatile Flow and Atherosclerosis in the Human Carotid Bifurcation - Positive Correlation between Plaque Location and Low and Oscillating Shear-Stress.* Arteriosclerosis, 1985. 5(3): p. 293-302.**

78. **S.Z. Zhao, B. Ariff, Q. Long, A.D. Hughes, S.A. Thom, A.V. Stanton, and X.Y. Xu, *Inter-individual variations in wall shear stress and mechanical stress distributions at the carotid artery bifurcation of healthy humans.* Journal of Biomechanics, 2002. 35(10): p. 1367-1377.**

79. **H.F. Younis, M.R. Kaazempur-Mofrad, R.C. Chan, A.G. Isasi, D.P. Hinton, A.H. Chau, L.A. Kim, and R.D. Kamm, *Hemodynamics and wall mechanics in human carotid bifurcation and its consequences for atherogenesis: investigation of inter-individual variation.* Biomechanics and Modeling in Mechanobiology, 2004. 3(1): p. 17-32.**

80. **T. Karino, H.L. Goldsmith, M. Motomiya, S. Mabuchi, and Y. Sohara, *Flow Patterns in Vessels of Simple and Complex Geometries.* Annals of the New York Academy of Sciences, 1987. 516: p. 422-441.**

81. D. Bluestein, P. Rissland, Y. Alemu, S. Einav, and J. Ricotta, *Abdominal Aortic Aneurysm Risk of Rupture: Patient-Specific FSI Simulations Using Anisotropic Model.* Journal of Biomechanical Engineering-Transactions of the Asme, 2009. 131(3).